NCHRP 12-68

FY 2004

Rotational Limits for Elastomeric Bearings

Final Report

APPENDIX D

John F. Stanton

Charles W. Roeder

Peter Mackenzie-Helnwein

Department of Civil and Environmental Engineering

University of Washington

Seattle, WA 98195-2700

TABLE OF CONTENTS

LIST OF FIGURES

LIST OF TABLES

APPENDIX D Test Results - Overview

D.1 Introduction

D.1.1 Arrangement of Test Series

A comprehensive program of 78 tests was conducted to evaluate the performance of elastomeric bearings under static and dynamic rotation. The complete test matrix is given in Table D-1, and detailed test results, including numerical values, for each individual test are provided in Appendix A.

The bearings were supplied by 4 different manufacturers, which are identified as manufacturers A, B, C, and D in the test matrix. In some cases, a manufacturer supplied several separate batches of bearings, delivered at different times, so the batch number is indicated by a number after the letter that defines the manufacturer. For example, A3 is the third order from manufacturer A. These four manufacturers are the major producers of steel reinforced elastomeric bearings in the US, and between them they produce 80 to 85% of the elastomeric bridge bearings used in this country.

Unless otherwise stated, all tests were conducted on "standard" bearings. These were selected because they are widely used in many states, and are therefore representative of field conditions. Their outer dimensions in plan were 22" x 9", they had three internal ½" thick rubber layers, four 11 gage shims, and top and bottom cover layers of 1/8" each. Thus the total thickness was approximately 2.23" and the shape factor was approximately 6. Edge cover was ¼". The elastomer was 50 durometer, temperature grade 3, Neoprene.

The main test program was divided into seven different test series, each of which is identified by a three-letter identification code (PMI, CYC, SHR, MAT, SHF, AST or PLT). Each test series was designed to provide quantitative data on the effects of that particular behavior, as discussed in greater detail below. For example, the CYC series was devoted to cyclic loading effects, and each test in it was conducted with a different combination of axial load and rotation. Comparisons between different test series permit the relative importance of the different behaviors to be evaluated.

Comparisons between bearings from different manufacturers were also conducted. The original goal contained in the research proposal had been to make the comparison by repeating a single test on bearings from different manufacturers. However, it became clear early in the work that significant differences existed, so the goal was expanded. In all, three monotonic tests (PMI 1a, PMI 1b and PMI 5) and five cyclic tests (CYC 5, CYC-7, CYC-9, CYC-11 and CYC-12) were conducted on bearings from each manufacturer.

Supplementary tests were also conducted to support the main series. Most of the supplementary tests consisted of material property or diagnostic tests.

This appendix provides a summary and evaluation of the test results. Section D.2 addresses the seven main test series that are defined in the test matrix. Section D.3

describes supplementary tests, such as material property tests, that were conducted to support the primary test series, and Section D.4 describes the analysis of the data. In Section D.5 the special issue of uplift and lift-off is discussed, and Section D.6 contains the conclusions from the entire Appendix.

Table D-1 Complete Bearing Test Matrix

Name	No.	Manufacturer/ Batch	Plan Dimensions	Aspect Ratio	Shape Factor	Material	Axial Stress	Static Rotation	Cyclic Rotation	Shear Disp.
PMI	1a	A1,A2,B1,C1,D1	9 x 22	2.44	6	CR50	step load			
PMI	1b	A1,A2,B1,C1,D1	9 x 22	2.44	6	CR50	cyclic to 8000psi			
PMI	1c	A2,B1	9 x 22	2.44	6	CR50	vary to fail	4%		
PMI	1d	A2,B1	9 x 22	2.44	6	CR50	cyclic to 8000psi	4%		
PMI	2	A1	9 x 22	2.44	6	CR50	2.5 GS	vary to 8%		
PMI	3	A1	9 x 22	2.44	6	CR50	3.5 GS	vary to 8%		
PMI	4	A1,A2,B1	9 x 22	2.44	6	CR50	3.0 GS	vary to 8%		
PMI	5	A1,A2,B1,C1,D1	9 x 22	2.44	6	CR50	4.0 GS	vary to 8%		
CYC	5	A1,A2,B1,C1,D1	9 x 22	2.44	6	CR50	5/8 P_0		6/8 θ_0	
CYC	7	A1,A2,B1,C1,D1	9 x 22	2.44	6	CR50	5/8 P_0		4/8 θ_0	
CYC	8	A1	9 x 22	2.44	6	CR50	5/8 P_0		2/8 θ_0	
CYC	9	A1,A2,B1,C1,D1	9 x 22	2.44	6	CR50	7/8 P_0		6/8 θ_0	
CYC	11	A1,A2,B1,C1,D1	9 x 22	2.44	6	CR50	7/8 P_0		4/8 θ_0	
CYC	12	A1,A2,B1,C1,D1	9 x 22	2.44	6	CR50	7/8 P_0		2/8 θ_0	
CYC	13	A1	9 x 22	2.44	6	CR50	5/8 P_0	2 ± 0.5%		
CYC	14	A1	9 x 22	2.44	6	CR50	5/8 P_0	2 ± 1.75%		
CYC	15	C1	9 x 22	2.44	6	CR50	7/8 P_0		0.005 rad	
SHR	1	B1	9 x 22	2.44	6	CR50	4.0 GS	vary to 8%		50%
SHR	2	B1	9 x 22	2.44	6	CR50	7/8 P_0		4/8 θ_0	70%
SHR	3	B1	9 x 22	2.44	6	CR50	7/8 P_0		4/8 θ_0	30%
SHR	4	B1	9 x 22	2.44	6	CR50	5/8 P_0		6/8 θ_0	30%
SHR	5	B1	9 x 22	2.44	6	CR50	7/8 P_0		6/8 θ_0	30%
SHR	6	A2	9 x 22	2.44	6	CR50	7/8 P_0		2/8 θ_0	30%
MAT	1	C2	9 x 22	2.44	6	CR60	5/8 P_0		6/8 θ_0	
MAT	2	C2	9 x 22	2.44	6	CR60	7/8 P_0		6/8 θ_0	
MAT	3	C2	9 x 22	2.44	6	CR60	7/8 P_0		4/8 θ_0	
SHF	1	C2	9 x 22	2.44	9	CR60	cyclic to 8000psi			
SHF	2	C2	9 x 22	2.44	12	CR60	cyclic to 8000psi			
SHF	3	C2	9 x 22	2.44	9	CR60	5/8 P_0		6/8 θ_0	
SHF	4	C2	9 x 22	2.44	9	CR60	7/8 P_0		6/8 θ_0	
SHF	5	C2	9 x 22	2.44	9	CR60	7/8 P_0		4/8 θ_0	
SHF	6	C2	9 x 22	2.44	12	CR60	5/8 P_0		6/8 θ_0	
ASR	1	C2	9 x 9	1	6	CR60	cyclic to 8000psi			
ASR	2	C2	9 x 9	1	6	CR60	5/8 P_0		6/8 θ_0	
ASR	3	C2	9 x 9	1	6	CR60	7/8 P_0		6/8 θ_0	
ASR	4	C2	9 x 9	1	6	CR60	7/8 P_0		4/8 θ_0	
PLT	1	A3 - sharp shim	9 x 22	2.44	6	CR50	5/8 P_0		6/8 θ_0	
PLT	2	A3 - sharp shim	9 x 22	2.44	6	CR50	7/8 P_0		6/8 θ_0	
PLT	3	A3 - deburred	9 x 22	2.44	6	CR50	5/8 P_0		6/8 θ_0	
PLT	4	A3 - deburred	9 x 22	2.44	6	CR50	7/8 P_0		6/8 θ_0	
PLT	5	A3 - rounded	9 x 22	2.44	6	CR50	5/8 P_0		6/8 θ_0	
PLT	6	A3 - rounded	9 x 22	2.44	6	CR50	7/8 P_0		6/8 θ_0	

D.1.2 Main Test Series – Definition and Goals

The seven main test series were:

- ***Series PMI:*** This series consisted of monotonic tests conducted on "standard" bearings with different combinations of axial force and rotation amplitude. The goal was to obtain points on an interaction diagram of axial force vs. rotation.

Such a diagram is similar to the interaction diagrams used for steel or concrete columns. Hence the series name of PMI.

- ***Series CYC:*** This series consisted of tests conducted on "standard" bearings with different combinations of constant axial force and cyclic rotation amplitude. The goals were to obtain points on a cyclic interaction diagram of axial force vs. rotation and to compare the effects of cyclic and monotonic rotation of the same amplitude. In most cases the mean rotation was zero, but in a few cases a constant offset rotation was applied in addition to the cyclic rotation, in which case the mean was non-zero. The goal of the latter tests was to investigate the effects of cyclic rotations due to traffic superimposed on a constant rotation caused by construction misalignment.
- ***Series SHR:*** The SHR Series tests were similar tests to the CYC series tests except that a constant shear deformation was applied to the bearing in addition to the axial load and cyclic rotation. In the field, bridge bearings experience axial, rotational and shear loading. Thus, it is important to evaluate the effects of combined loading.
- ***Series MAT:*** Most bearings used in this research program employed the same nominal 50 Shore A durometer, Neoprene, elastomer compound. In the MAT series a different elastomer, with a 60 Shore A hardness, was used to determine the effect of material properties. The 60 durometer material was expected to resist axial force better, because the strains induced would be smaller. However, the additional stiffness might lead more readily to lift-off in rotation, which might cause damage more quickly. 60 durometer material is quite commonly used for bearings.
- ***Series SHF:*** The standard test bearings were 9x22 bearings with a shape factor of 6. In the SHF ("SHape Factor") series, bearings with shape factors of 9 and 12 were tested. The external dimensions of the bearings were kept the same, but the internal rubber layer thickness was changed to increase the shape factor. The axial load and rotation were adjusted so that they produced the same theoretical shear strain as in the comparable tests with a standard bearing. Because a higher shape factor generally means that the bearing can accommodate a higher axial load but less rotation, the necessary adjustments consisted of in creasing the axial load and reducing the rotation used in the test. If the linear theory for bearings is correct, the higher shape factor bearing should experience the same strains, and therefore exhibit the same damage, as the standard bearings in the CYC tests.
- ***Series ASR:*** All the standard bearings were 9" x 22" in plan. However, theory shows that the aspect ratio influences the shear strains, even though the load and shape factor are held constant. Therefore some bearings were tested that had a different plan shape but retained the same shape factor of 6. This was achieved by adjusting the thickness of the internal layers.
- ***Series PLT:*** This final test series was added during the course of the research in response to information gained from a pilot test series, for which the specimens had sharp edges as a result of machining. In them, the elastomer debonded faster

than it did in the standard tests under the same cyclic rotation regime. This observation suggested that the shape of the shim edge influenced the cyclic loading capacity, so three sets of bearings were prepared and tested to investigate the issue. One set had as-sheared edges, in the second the edges were de-burred with a belt-sander after shearing, and in the third the edges were rounded to a perfectly circular profile using machine tools.

D.2 Main Test Series

D.2.1 PMI Test Series

In the PMI series of tests, each bearing was subjected to a constant axial load and a single cycle of rotation to the rotational rig rotation limit of approximately ±0.08 radians. The primary goal of these tests was to establish an axial load vs. rotation interaction curve for the standard bearings. To do so, a criterion for failure is necessary, and the length of debonding was used here. It was measured in inches along the long sides of the bearing, at the center two shims. (The debonding at the outer two shims was not visible, because it was obscured by the keeper plates of the rig that were needed to prevent the bearing from slipping out of place). Furthermore, the initial debonding always occurred at one of the center shims, and the majority of all debonding was concentrated there

For convenience the tests included in the PMI test series are reproduced in

Table D-2. The series started with tests under axial load alone, to find the approximate level of load to be applied in the subsequent tests that included rotation. Two monotonic loading regimes were used. In the first, test PMI-1a, the load was increased in steps of approximately 59 kip (600 psi), and the load was held constant at this load level for approximately 5 minutes. The pause allowed time for detailed inspection of the bearing, and it permitted investigation of the visco-elastic (creep) characteristics of the bearing, while allowing time required for crack initiation in the material. The 600 psi load increment was chosen because it represented approximately 1.0*GS*. Loading in terms of *GS* was considered appropriate because the current AASHTO LRFD design code calculates the axial load limits in terms of *GS* (AASHTO, 2005). Linearized theory (Gent, and Meinecke, 1970, Lindley, 1979), shows that an axial stress of *GS* leads to a peak nominal shear strain, γ_a, of 1.0, if the approximations of $\gamma_a = 6S\varepsilon_c$ and $e_c = \sigma_c/6GS$ are used.

Table D-2 Series PMI Test Matrix

Name	No.	Manufacturer/ Batch	Plan Dimensions	Aspect Ratio	Shape Factor	Material	Axial Stress	Static Rotation	Cyclic Rotation	Shear Disp.
PMI	1a	A1,A2,B1,C1,D1	9 x 22	2.44	6	CR50	step load			
PMI	1b	A1,A2,B1,C1,D1	9 x 22	2.44	6	CR50	cyclic to 8000psi			
PMI	1c	A2,B1	9 x 22	2.44	6	CR50	vary to fail	4%		
PMI	1d	A2,B1	9 x 22	2.44	6	CR50	cyclic to 8000psi	4%		
PMI	2	A1	9 x 22	2.44	6	CR50	2.5 GS	vary to 8%		
PMI	3	A1	9 x 22	2.44	6	CR50	3.5 GS	vary to 8%		
PMI	4	A1,A2,B1	9 x 22	2.44	6	CR50	3.0 GS	vary to 8%		
PMI	5	A1,A2,B1,C1,D1	9 x 22	2.44	6	CR50	4.0 GS	vary to 8%		

In the second loading regime used (tests PMI-1b), the loading was increased gradually and continuously to 8000 psi, after which it was released. That load cycle was then repeated up to 20 times. This loading regime was not strictly monotonic, but it was used because some bearings did not exhibit any damage with the step load method.

D.2.1.1 Axial Step Load Test (PMI 1a)

The first axial step load test was performed on a bearing from the first batch of bearings purchased from Manufacturer A (Specimen PM1-1a-A1). Figure D-1shows the load versus displacement graph for this specimen. The compressive load was divided by the total area of the bearing to give the average stress, and the displacement was taken to be the average of the two potentiometer displacements, one on either side. In test PMI-1a-A1 debonding started in the center of the long side of the bearing at a compressive stress of 3000 psi. This load was chosen to be the reference load, called P_0, that would be the basis of the loads used in the other tests. This choice provides a somewhat conservative estimate of P_0 as can be seen in the summary of the axial step load test data in Table D-3, because the bearings on which it was based had shims with edges that were machined square. (The machining was necessary to provide the shims with a special, non-rectangular shape that was needed to allow torsion tests to be conducted successfully. The torsion tests are described in Section D.3.2. They were eventually abandoned because they did not provide the information hoped for. The fact that the sharp, machined edges would hasten the start of debonding was not discovered until several tests had been finished, but which time it was too late to change the P_0 value that had been selected).

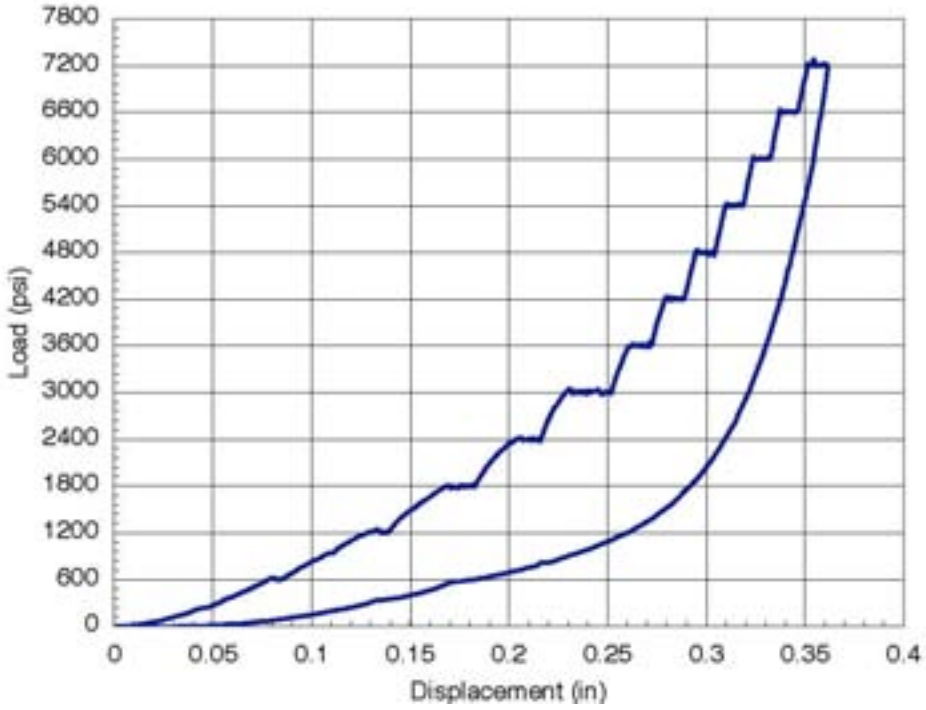

Figure D-1. Typical Load vs. Displacement Graph for Axial Step Load Tests

Two PMI-1a bearings developed debonding during the step test and two others did not as summarized in Table D-3. The percentage of debonding provided in Table D-3 is the length of debonding measured in inches along both sides of the center two shims, divided by the total length of the long edges of the shims (88 inches).

Table D-3 Test PMI1a. Stress at Initial Debonding and Total Debonding at 6000 psi

Bearing	Stress at Initial Debonding (psi)	Debonding at 6000 psi (%)	Stress at Plate Fracture (psi)
A1	3,000	10	–
A2	4,200	2	10,100
B1	–	0	11,900
C1	7,200	0.5	–
D1	–	0	–

Once the step-loading test was complete, PMI-1a bearings A2, B1, C1, and D1 were loaded to the machine capacity (2,400 kips, or approximately 12 ksi average stress). Bearings A2 and B1 failed by shim fracture at 10.1 and 11.9 ksi respectively, while bearings C1 and D1 did not fail. Both failures were characterized by tensile fracture of the steel plates along the centerline of the bearing, as shown in Figure D-2. As the rubber bulged out laterally, it pulled outwards on the shim plates and eventually fractured the plates. The axial stress at fracture of the shims is approximately ten times the maximum axial stress on a typical bearing with current service design loads and twice the strength of the concrete in the supporting structure. Therefore shim fracture is a mode of failure that occurs eventually, but at a load so high that it has limited relevance to the field performance.

a) Bearing Prior to Removal from Test Frame

b) Bearing After Removal from Test Frame

Figure D-2. Shim Fracture of Specimen PMI-1a-B1

D.2.1.2 PMI-1b-Cyclic Axial Tests

The PMI-1a tests did not cause damage in all bearings nor did they provide a continuous load-displacement curve. The PMI-1b tests were designed to do both. The PMI-1b tests consisted of repeated axial loads to a stress of 8,000 psi until damage was observed. Each cycle used approximately one minute to apply the load, one minute to photograph and

check the bearing for damage and one minute to unload. The repeated load caused damage to all the bearings, and they are compared in Table D-4

Table D-4. Rate of Debonding for PMI-1b Tests

Debonding	A1	A2	B1	C1	D1
Initial	1	4	3	2	5
25%	1	9	4	–	13
50%	1	15	–	–	–
75%	8	20	–	–	–
100%	40	–	–	–	–
Total Cycles	50	20	30	13	13

The table shows the number of cycles required for each specimen to reach various levels of debonding. PMI-1B-A1 was the only bearing to initiate debonding on first cycle and it progressed more than any other bearing until it was fully debonded at 40 cycles. However, this bearing had machined shims with sharp edges. Specimen PMI-1b-A2 was also fabricated by manufacturer A, but its shims had been de-burred with a belt-sander. Its better performance shows the effect of sharp shim edges.

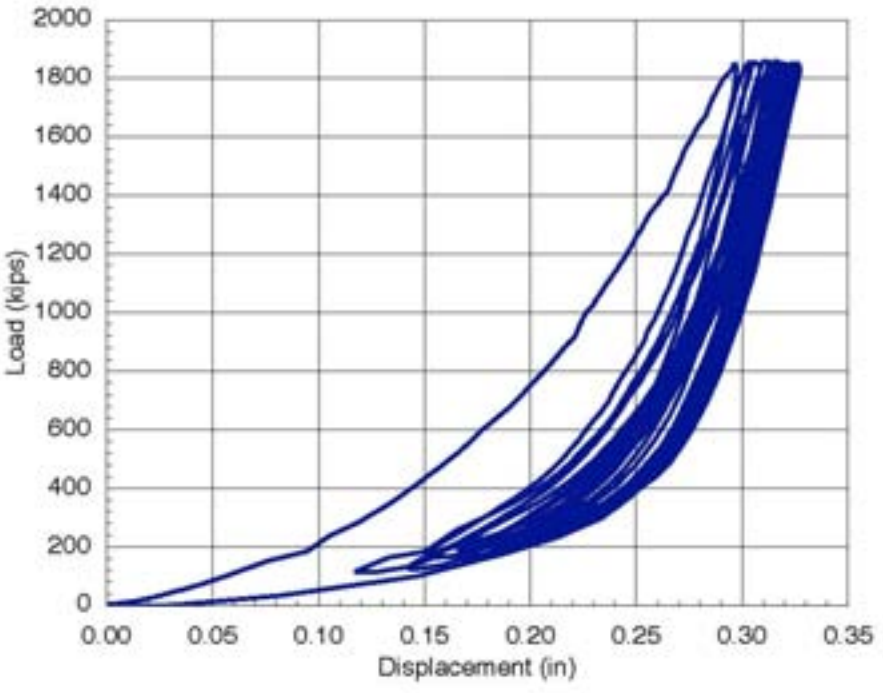

Figure D-3. Typical Load vs. Displacement for PMI-1b Tests (PMI-1b-C1)

Figure D-3 shows typical load-displacement behavior for the cyclic axial tests. The bearing stiffened with increasing stress, as is typical of the load-displacement behavior of elastomeric bearings, but the bearing also relaxed slightly with increasing cycles, resulting in a larger total displacement. This growth in displacement was attributed to a combination of accumulated damage and change in material properties as any residual crystallization was removed by the work done on the bearing. The change in total displacement for each cycle decreased as the test progressed until the bearing essentially began retracing the path of the previous cycle but there was no consistent pattern to the stiffness loss as the cycles progressed. Figure D-4 shows the instantaneous tangent stiffness at various loads and cycles throughout the test. The scatter was greater at higher loads, but there was no overall trend toward stiffness loss.

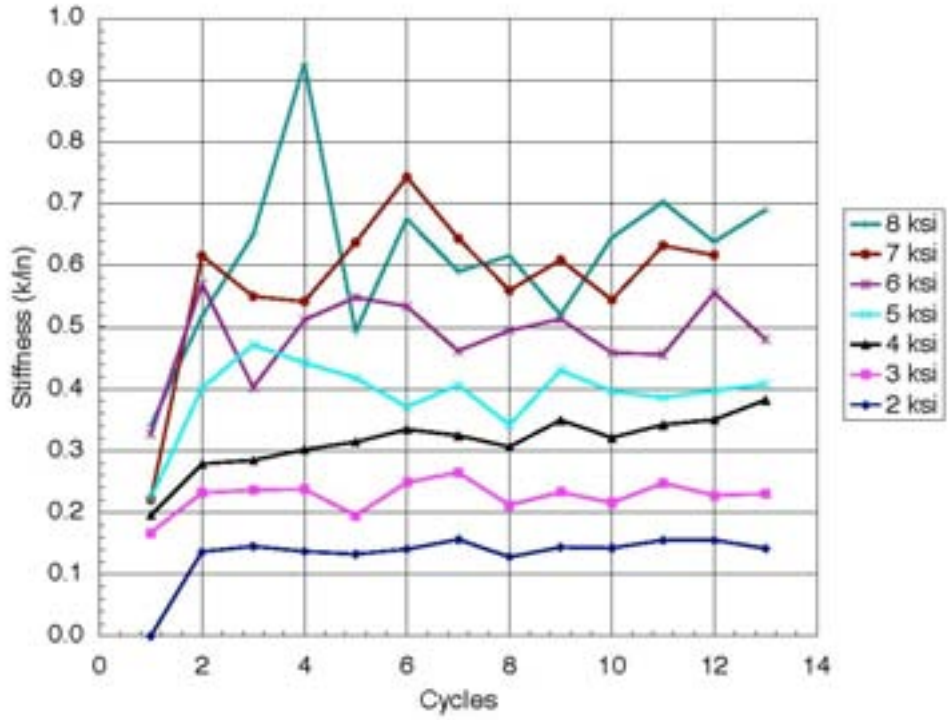

Figure D-4. Instantaneous Tangent Stiffness during Test PMI-1b-C1

Unlike the damage measurements, which varied significantly between manufacturers, the first cycle load-displacement behavior was quite consistent between the five bearings tested, as shown in Figure D-5.

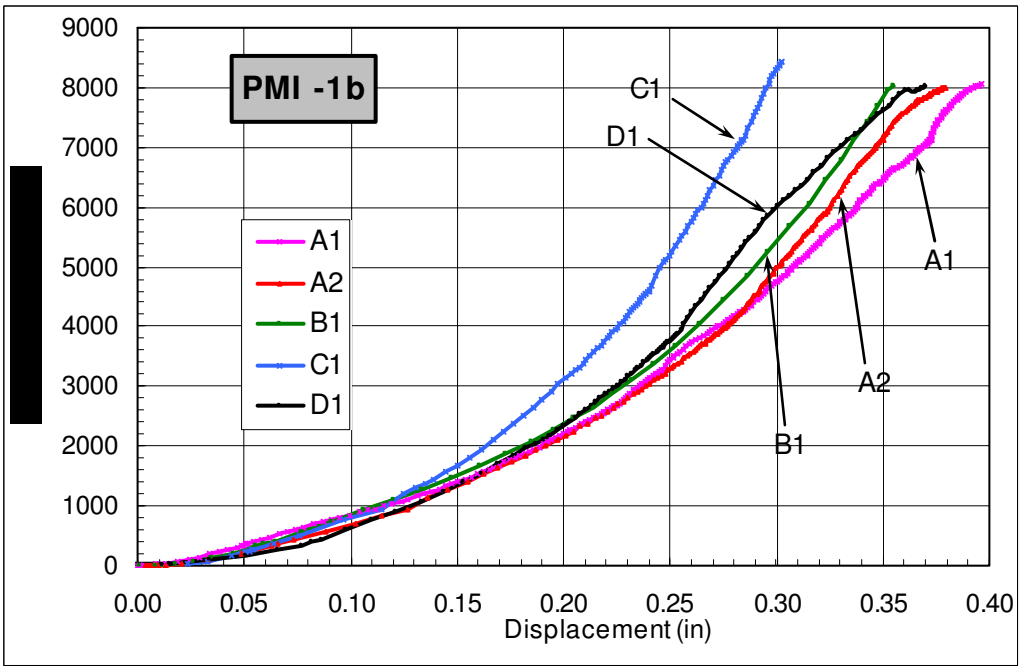

Figure D-5. Axial Load-Displacement Curves, Tests PMI-1b

D.2.1.3 PMI-1c and PMI-1d – Axial Tests with Constant Rotation

Monotonic step load tests (PMI-1c) and cyclic (PMI-1d) axial tests were done on A2 and B1 bearings with tapered plates to impose a fixed rotation of 0.04 radians. In the monotonic step load tests, the A2 bearing started debonding at 4200 psi when tested between parallel plates, but did not start debonding until 8000 psi when tested between tapered plates as shown in Table D-5. This result is counter-intuitive, and suggests that the initiation of debonding is an event with which considerable scatter is associated. However, the total extent of debonding was greater in the tapered plate test. The B1 bearing behaved more as expected: it showed no debonding in the parallel plate test, but it debonded at 2500 psi in the tapered plate test.

Table D-5. Stress Level at Initiation of Debonding with (PMI-1c) and without (PMI-1a) Rotation

	Axial only		With 0.04 rad rotation	
Bearing	Stress at initial debonding (psi)	Total debonding (%)	Stress at initial debonding (psi)	Total debonding (%)
A2	4200	2	8000	25
B1	–	0	2500	25

These apparent inconsistencies illustrate the main problem of using initiation of debonding as a measure of the bearing's resistance to damage. Debonding starts at the point where the local stress or strain demand first exceeds the local capacity. However

the local capacity may vary with weak spots distributed along the rubber-steel interface, because of variability of materials and the manufacturing process. Therefore, considerable scatter must be expected in the load at first debonding, and the loading needed to reach some higher level, say 25% debonding, may be a more consistent indicator of the bearing's susceptibility to damage.

In the cyclic tests the load was cycled between 0 and 8000 psi as with the PMI-1b series, but with the tapered plates in place. The number of cycles required to reach different levels of debonding, is presented in Table D-6. The cyclic tests were first tried with smooth steel tapered plates, but the bearings slipped out from between them at relatively low loads. As a result, a lip was attached to the tapered plates to inhibit slip. The tests reported here were conducted with the latter configuration. Despite this precaution, the bearings still slipped out of place, riding over the lip on the plates as shown in Figure D-6. Consequently, obtaining reliable data from these cyclic tests was difficult.

Table D-6. Comparison of Debonding with (PMI01d) and without (PMI-1b) Rotation

	Axial only		With 0.04 rad rotation	
Debonding	A2	B1	A2	B1
Initial	4	3	1	2
25%	9	4	1	–
50%	15	–	1	–
75%	20	–	4	–
100%	–	–	–	–
Total Cycles	20	30	6	13

Figure D-6. Bearing Slips out of Tapered Plates during Test

The A2 bearing debonded more rapidly and more extensively when the tapered plates were used than did its counterpart tested between parallel plates. This is as might be expected. The B2 bearings both showed very little debonding, and permitted no firm conclusion to be drawn.

The evidence from debonding therefore suggests that there is a slight tendency to sustain damage earlier when axial load and rotation are applied simultaneously, but significant

scatter is present and it masks any strong trend. However analysis of the load-displacement data in Figure D-7 reveals an overall axial softening of the system when a fixed rotation was added to the cyclic axial load application. During the first cycle, the bearings with and without the imposed rotation followed much the same load path, but thereafter the displacements increased more rapidly in the bearing tested with the tapered plate.

The instantaneous stiffness of the entire bearing was calculated at various loads for each cycle. Then all values for each load from all cycles were averaged to get an average tangent stiffness for the bearing at a given load. Figure D-8 shows these average stiffnesses for A2 and B1 bearings with and without the imposed rotation. On average, 0.04 rad rotation reduces the axial stiffness of the A2 bearing by 10% and that of the B1 bearing by 5% or less. These results should be evaluated in light of the fact that the parallel- and tapered-plate tests were conducted on different bearings from the same batch (A2 or B1). Although the bearings in the pairs were nominally identical, some minor differences in stiffness are possible. At low loads, the bearing makes only partial contact with the tapered plates and so should be expected to display a lower stiffness. At 0.04 radians rotation with full contact, the centerline of the bearing needs to be compressed by a distance of at least 0.04 * 9/2 in = 0.18 in. Figure D-8 shows that this occurs at an average stress of approximately 2 ksi. Therefore, all of the values shown in Figure D-8 correspond to the full contact condition,

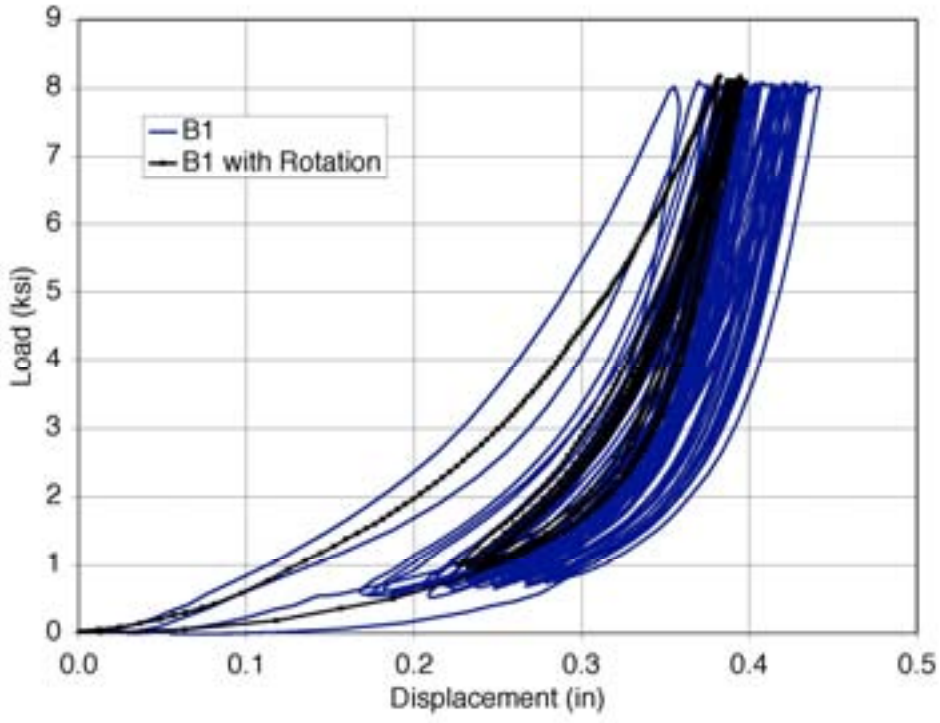

Figure D-7. Load/Displacement for Axial Test with and without 0.04 Imposed Rotation

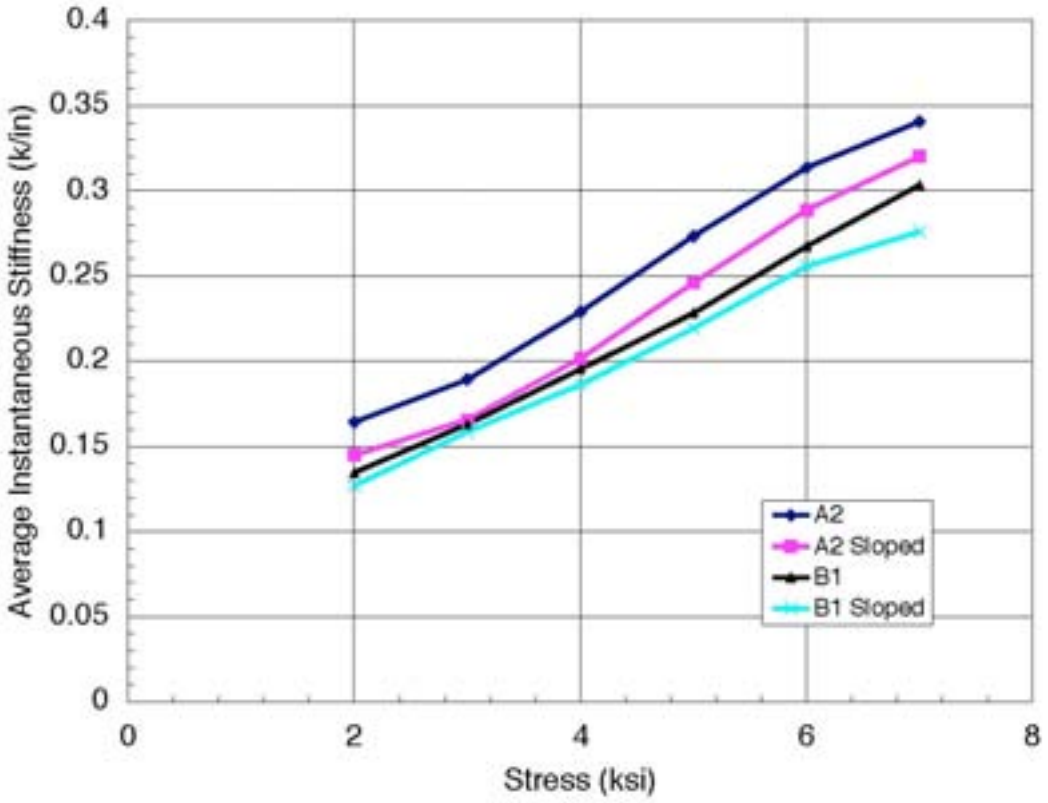

Figure D-8. Instantaneous Stiffness at Various Loads Averaged overall all Load Cycles

D.2.1.4 PMI-2 through PMI-5 – Monotonic Rotation Tests

Monotonic rotation tests were conducted in the multi-load rotation rig to determine the rotation, θ_0, at which debonding damage started as a function of axial load or compressive stress level. This rotation was then used as a reference value. In the CYC test series, the cyclic rotations were chosen as proportions of the reference value.

PMI-4-A1 was the first monotonic rotation test and it started to debond upon application of the axial load, but additional debonding was not detected until the rotation was 0.05 radians. This value was the smallest monotonic rotation at which debonding started in any bearing, and 0.05 radians was chosen as θ_0 for all subsequent cyclic tests. Because the Batch A1 bearings had shims with sharp milled edges, an argument can be made for ignoring these data as will be discussed later in this appendix. However, they are included here in the interests of completeness.

Monotonic tests were performed for all bearings in tests PMI-2 through PMI-5 at different compressive stress levels as shown in

Table D-2. Table D-7 shows the rotation θ_0 at initiation of debonding in these tests. Some tests exhibited no debonding during the initial monotonic rotation of 0.08 radians and a reversed monotonic rotation was applied. Those tests in the table with negative values for the debonding rotation showed no initiation of debonding during the initial

rotation cycle and the negative number is the reverse rotation where debonding was observed.

Table D-7. Rotation at Initiation of Debonding During Monotonic Rotation Tests

Test	PMI2	PMI3	PMI4			PMI5				
	A1	A1	A1	A2	B1	A1	A2	B1	C1	D1
Rotation (rad)	0.05	0.08	0.05	0.06	-0.08	0.01	0.06	-0.08	0.08	-0.01

From these data, an axial compressive stress vs. rotation per layer interaction plot was made and is given in Figure D-9. This plot contains all data on initial debonding from all PMI tests, including the compressive tests and tapered plate tests. In general, tests with lower axial loads reached higher rotations before debonding started Best fit lines for A1 tests and all the other tests are provided. The A1 tests were separated from all other tests because of the sharp edges on the steel shims. While there are clear trends shown in the figure, a usable interaction curve was not immediately apparent. It is worth noting that both the axial stresses and the rotations used here are significantly higher than those expected in the field.

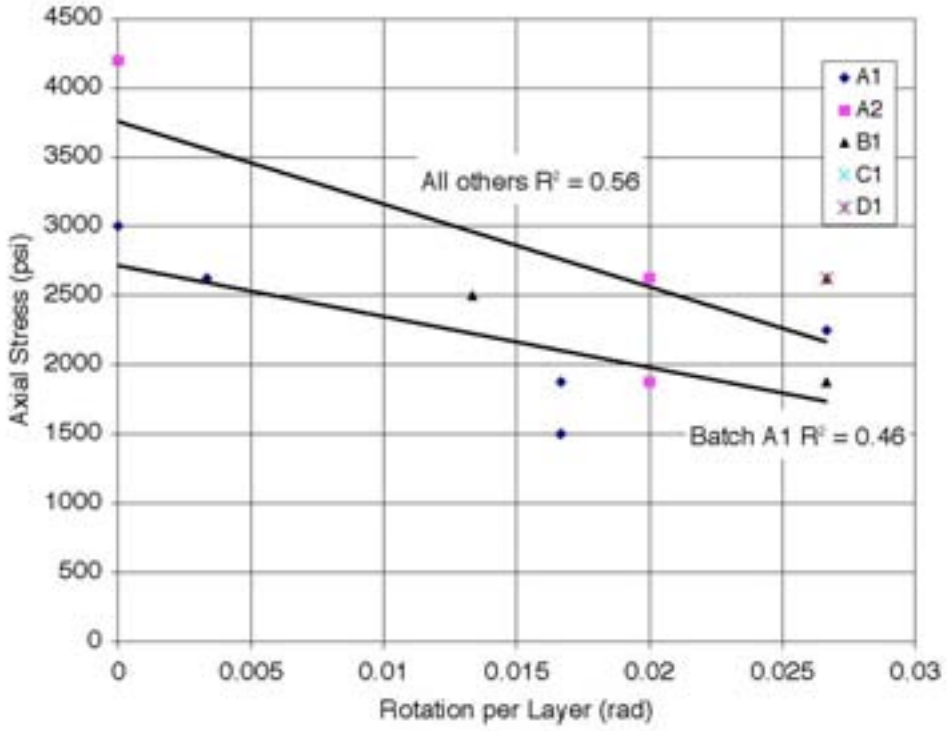

Figure D-9. Compressive Stress vs. Rotation at First Debonding for all PMI Tests

Estimating damage at high rotations was very difficult. Under high rotations, the shims moved laterally (vertically in the test rig) as seen in Figure D-10. This phenomenon was referred to as the "watermelon seed effect" because the shims appeared to be squeezed out by the combination of axial pressure and rotation, simulating the behavior of a watermelon seed squeezed between finger and thumb. This phenomenon caused the bulges to appear clean on the edge being pulled in and they disappeared from the other, hiding the damage in both cases as seen in Figure D-10 and Figure D-11. To get a more accurate gauge of debonding in tests PMI-5-C1 and PMI-5-D1, the loading was paused, returned to zero rotation to take measurements, and then returned to its rotated state to resume the test.

Figure D-10. Photo of the "Watermelon Seed" Effect

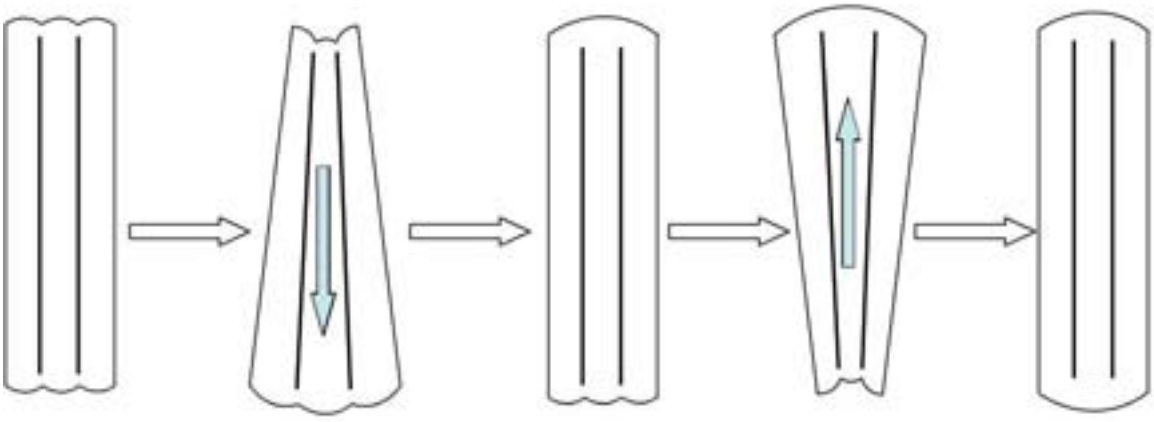

Figure D-11. Progression of Debonding Hidden by "Watermelon Seed" Effect

The bulge height was also measured for all tests, since it is approximately related to the shear strain in the elastomer. This information is included in the detailed test data for all specimens in Appendix A. The bulge heights were originally measured to gauge whether debonding had occurred, but it soon became apparent that the presence of a bulge could be detected much more quickly and easily by running a finger along the shim edge. The value of depth gauge measurements was further decreased with the addition of the holding plates or restrainer bars described in Section C1.4, because the original outer measuring points, over the outer shims, were no longer accessible. Consequently, the outer points were then measured as close to the edge as possible, touching the holder plates, meaning that the height was measured at the peak of the bulge, but not at a point over the end of a plate.

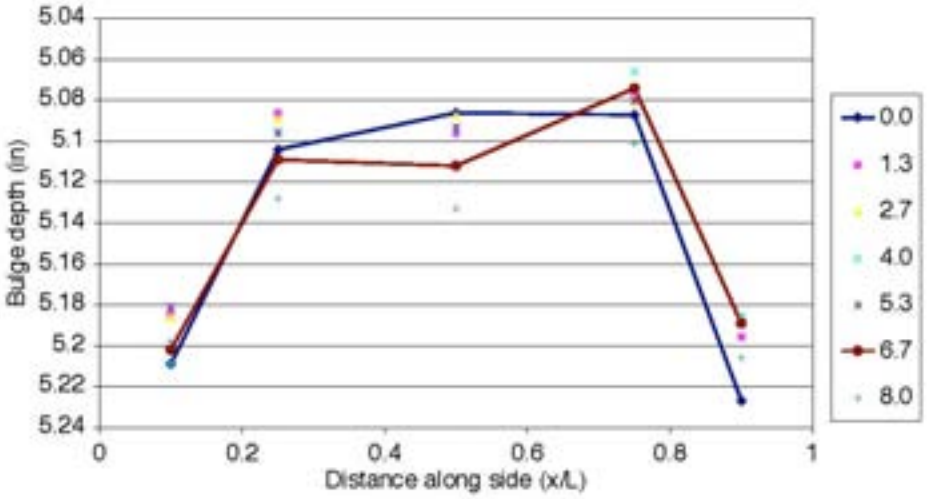

Figure D-12. Raw Bulge Data for Different Rotation Angles

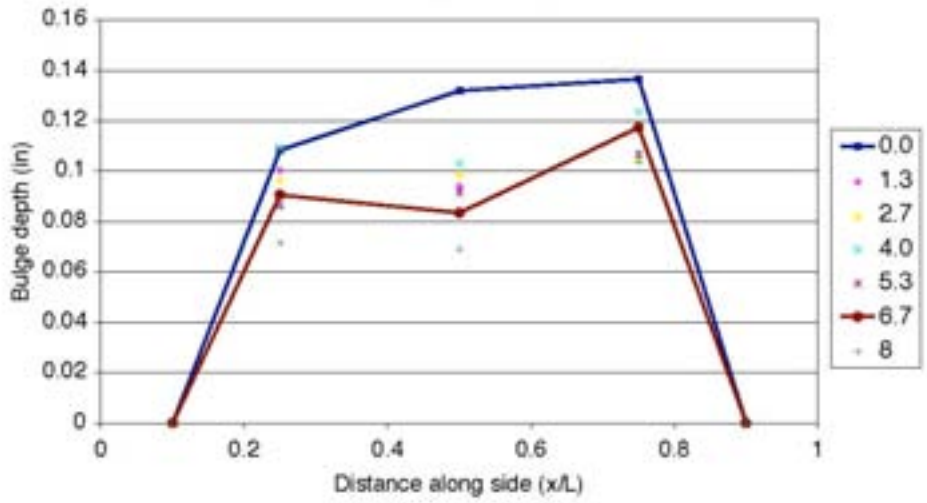

Figure D-13. Relative Bulge Height for Different Rotation Angles.

Depth gauge data may still used to calibrate finite element models of bearings to verify that the bulges are of similar size, so they are included here for reference. The measurements were taken at 5 points across the centerline of the bearing on both the top and bottom. These results were then tabulated as raw data to verify that they followed the general bulge pattern as shown in Figure D-12

The bulge heights were then computed relative to a chord between the two faces of the bearing by subtraction of the chord measurements, and typical relative bulge heights are shown in Figure D-13. These heights were then plotted against the rotation angle in radians, or total number of cycles for the cyclic rotation tests, to produce the graphs in Appendix A.

D.2.2 CYC Test Series

The CYC test series was a primary focus of the research program, because it was used to study combinations of different strains and loads and the effect of multiple load cycles on bearing performance. The tests are accelerated tests in which the applied loads and rotations were much higher than those expected in the field, in order to induce damage, and therefore judge the relative importance of the different variables in a period of days or weeks. The results of these tests serve as the basis for many of the proposed design provisions developed in Appendix F. The cyclic tests were time consuming, because some individual tests took weeks to reach significant damage levels and a number of tests were performed. All data from each test can be found in Appendix A, including debonding progression graphs, bulge height graphs, and stiffness and energy dissipation plots.

Table D-8 summarizes the test matrix for this portion of the research program. As can be seen, five of the tests were conducted on bearings from all four manufacturers. Test CYC-8 was not used in this set because the loading was so light that damage accumulated only very slowly.

Table D-8. CYC Test Matrix

Name	No.	Manufacturer/ Batch	Plan Dimensions	Aspect Ratio	Shape Factor	Material	Axial Stress	Static Rotation	Cyclic Rotation	Shear Disp.
CYC	5	A1,A2,B1,C1,D1	9 x 22	2.44	6	CR50	5/8 P_0		6/8 θ_0	
CYC	7	A1,A2,B1,C1,D1	9 x 22	2.44	6	CR50	5/8 P_0		4/8 θ_0	
CYC	8	A1	9 x 22	2.44	6	CR50	5/8 P_0		2/8 θ_0	
CYC	9	A1,A2,B1,C1,D1	9 x 22	2.44	6	CR50	7/8 P_0		6/8 θ_0	
CYC	11	A1,A2,B1,C1,D1	9 x 22	2.44	6	CR50	7/8 P_0		4/8 θ_0	
CYC	12	A1,A2,B1,C1,D1	9 x 22	2.44	6	CR50	7/8 P_0		2/8 θ_0	
CYC	13	A1	9 x 22	2.44	6	CR50	5/8 P_0	2 ± 0.5%		
CYC	14	A1	9 x 22	2.44	6	CR50	5/8 P_0	2 ± 1.75%		
CYC	15	C1	9 x 22	2.44	6	CR50	7/8 P_0		0.005 rad	

D.2.2.1 Debonding Failure Mode

The primary measure of bearing degradation was the amount of debonding observed as the test progressed. Debonding is the separation of the rubber layer from the shim, resulting in a bulge along the line of the shim where there was formerly a recess on the

bearing surface, as shown in the photo of Figure D-14. Debonding always started with a tension failure of the bond between the cover rubber and the outer face of the shim as depicted in the photo of Figure D-16. This initial tensile separation may or may not be observable on the surface of the bearing, and it appeared to have little impact upon bearing performance. Under further loading, delamination, or shear failure near the interface of the rubber and the flat surface of the shim, occurred, causing a surface bulge as shown in Figure D-15. The bearing shown in Figure D-15 is the same bearing as shown in Figure D-14, but the photo is taken later in the test. Distorted bulging caused by delamination can be seen in the right central portion of the photo.

In this report, the word *debonding* is henceforth used to define the tensile separation of the elastomer from the edge of the shim, while *delamination* defines the separation from the flat surface, caused by shear stress. If the internal mechanism is unknown, the process is referred to in this report as *debonding*. In most cases it is difficult to distinguish the two just by looking at the outside of the bearing. However, the distinction is made because debonding is a local effect that has no discernible effect on the bearing performance, while delamination starts to render the bearing more flexible in compression. Delamination has to be severe for the compressive stiffness to become small enough to lead to a noticeable reduction in serviceability. However, it has other damaging effects as well, such as causing stress concentrations at the tip of the crack which could cause rapid propagation, and eventual tearing apart of the bearing, under cyclic shear displacements.

Figure D-14. Photo of Bearing Bulge Pattern Prior to Damage

Figure D-15. Debonding Visible at Surface of Bearing

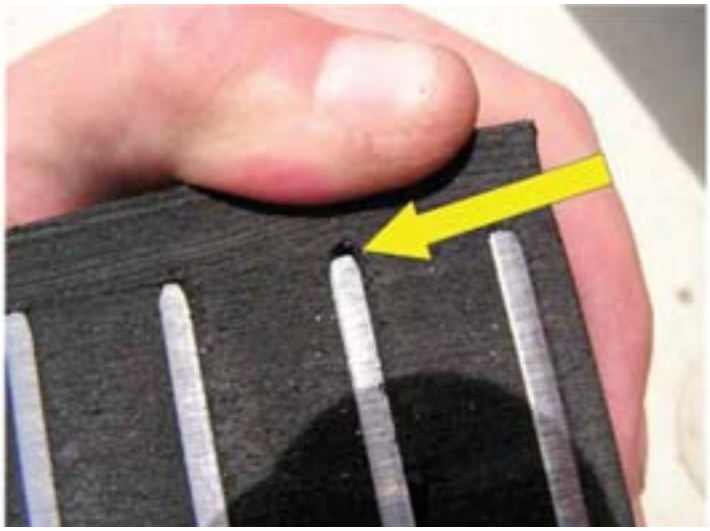

Figure D-16. Photo of Tensile Separation at the Edge of the Shim (Bearing Batch A2)

The length of debonding was recorded along each shim. This measurement is approximate because the extent of the separation can only be approximately determined by surface measurements. As a result, the length was measured to the nearest inch. There were four shims in each bearing but only the debonding along the center two shims was recorded because the holding plates or restrainers obscured the two outer shims. Thus, total debonding length for a given bearing was 88 inches (22 inches per plate, two plates and two faces). In the discussion that follows, debonding is often expressed as a percentage of the 88-inch total length

Table D-8 shows that the CYC tests were performed at different compressive stress levels and cyclic rotation amplitudes. The compressive loads are expressed in terms of the load P_0 (and in some cases as multiples of GS), because prior research has shown that GS is approximately related to the strain level of the elastomer. The cyclic rotation was correlated to the static rotational limit, θ_0, defined in the PMI tests. Table D-9 translates these relative numbers into specific numerical values.

Five tests were performed on bearings from of each the four manufacturers, including both batches from Manufacturer A. Figure D-17 through Figure D-21 show the progression of debonding as a function of the cycle number for four bearing batches (excluding Batch A1, which had the sharp-edge shims).

Table D-9. Summary of CYC Test Loads

	CYC5	CYC7	CYC9	CYC11	CYC12	
Axial load	$^{5}/_{9}P_0$ 1875psi	$^{5}/_{9}P_0$ 1875	$^{7}/_{9}P_0$ 2625	$^{7}/_{9}P_0$ 2625	$^{7}/_{9}P_0$ 2625	psi
Rotation angle	$^{5}/_{9}\theta_0$ 3.75	$^{4}/_{9}\theta_0$ 2.5	$^{5}/_{9}\theta_0$ 3.75	$^{4}/_{9}\theta_0$ 2.5	$^{2}/_{9}\theta_0$ 1.25	10^{-3} rad

Figure D-1 through Figure D-21 plot the percentage of debonded length against number of cycles. The horizontal scale varies between the figures. These figures show several consistent trends, but also show scatter in the results. In general, increasing axial load and increasing cyclic rotation resulted in more rapid and more extensive debonding than did smaller loads and rotations. Comparison of Figure D-17 and Figure D-18 shows that debonding rate was 2 to 3 times more rapid when the cyclic rotation was increased from 0.025 radians ($1/2\theta_0$) to 0.0375 radians ($3/4\theta_0$) and the axial stress was 1875 psi in both cases. Figure D-19, Figure D-20 and Figure D-21 show similar results. These figures show the results of tests completed at an axial compressive stress of 2625 psi, but with different rotation amplitudes. Increased rotation significantly decreases the number of cycles needed to achieve a given damage level. Comparison of Figure D-17 and Figure D-19 show that increasing the axial stress level while maintaining the same cyclic rotation also leads to an increased rate of debonding in the bearing. Comparison of Figure D-18 and Figure D-20 lead to similar observations. These observations are clearly consistent with the strain-based design limits commonly used for elastomeric bearing design.

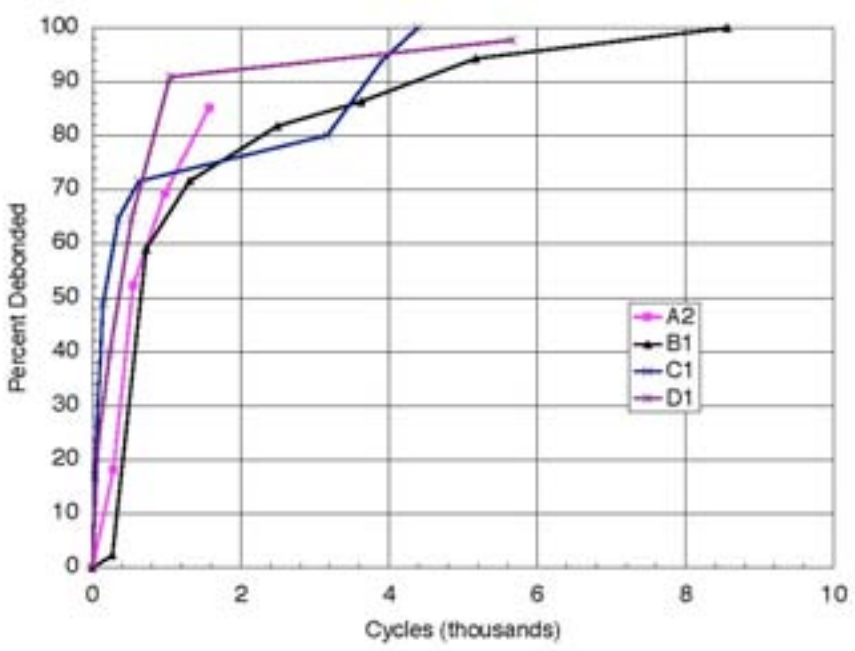

Figure D-17. Debonding vs. Cycle Number. Test CYC-5 ($^5/_8P_0$, $^3/_4\theta_0$)

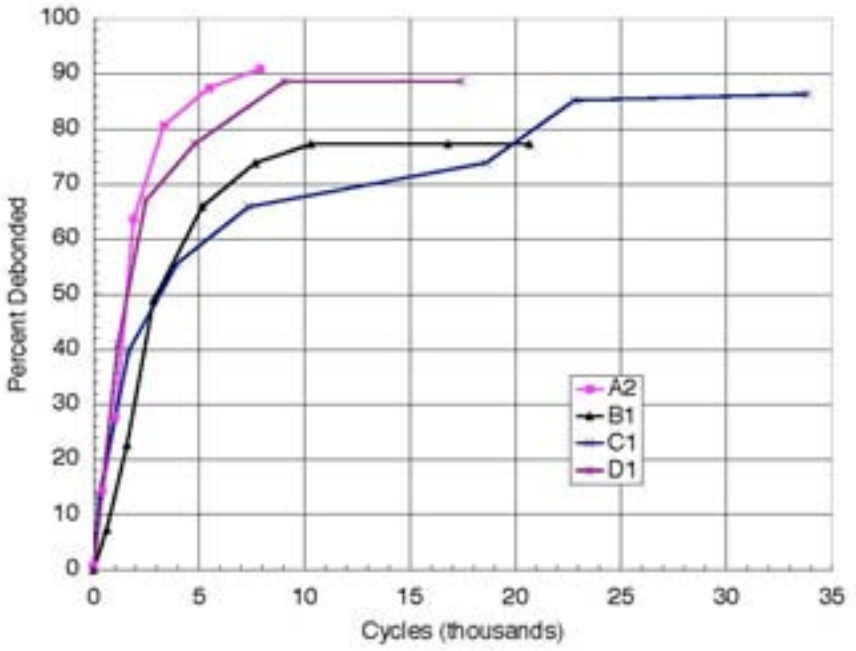

Figure D-18. Debonding vs. Cycle Number. Test CYC-7 ($^5/_8P_0$, $\frac{1}{2}\theta_0$)

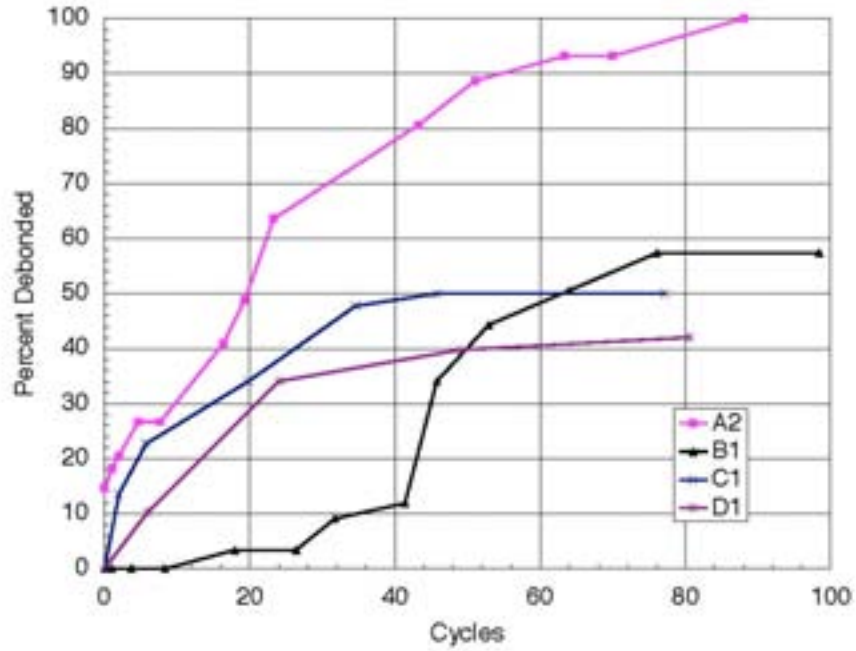

Figure D-19. Debonding vs. Cycle Number. Test CYC-9 ($^7/_8P_0$, $^3/_4\theta_0$)

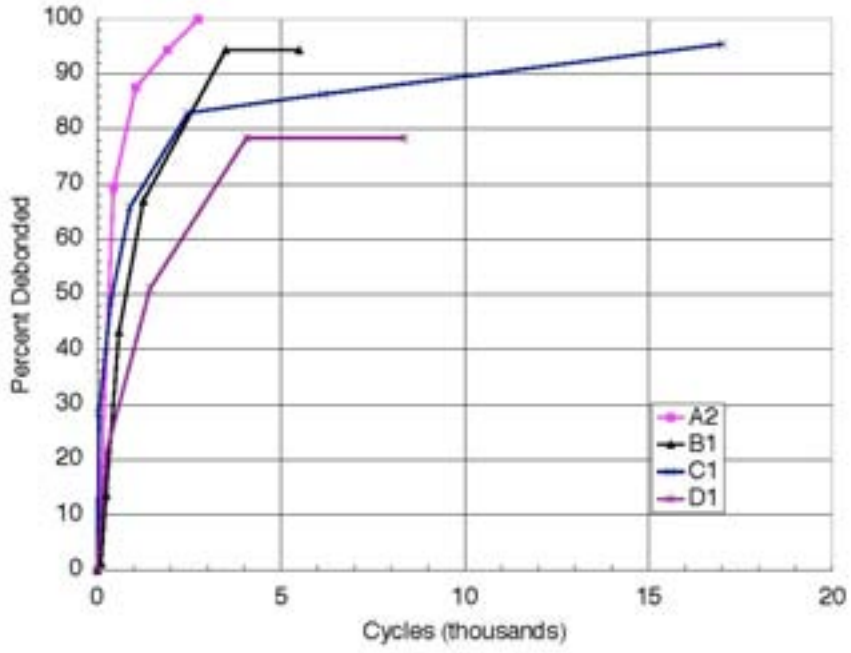

Figure D-20. Debonding vs. Cycle Number. Test CYC-11 ($^{7}/_{8}P_0$, $\frac{1}{2}\theta_0$)

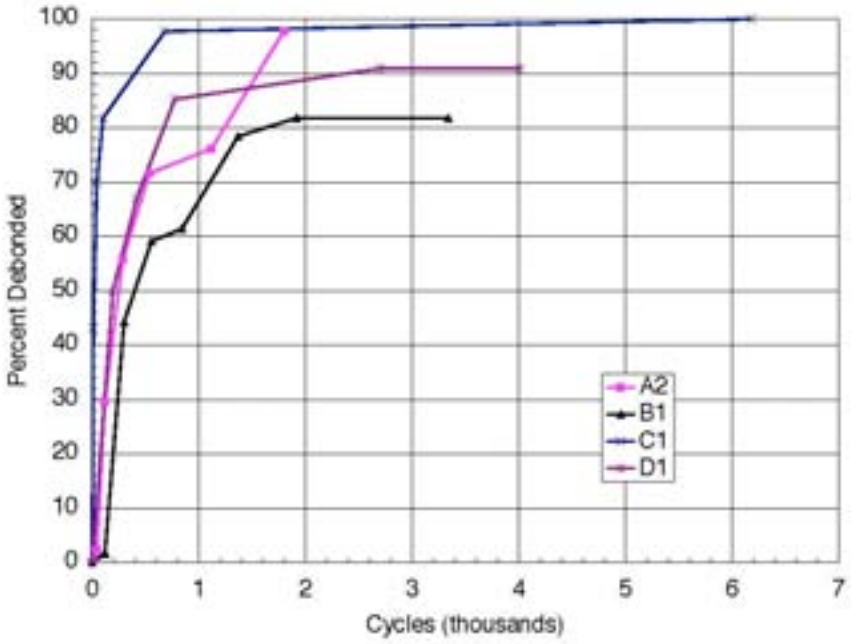

Figure D-21. Debonding vs. Cycle Number. Test CYC-12 ($^{7}/_{8}P_0 < {}^{1}/_{4}\theta_0$)

While clear trends exist within the cyclic test results, scatter among the results is also apparent. The individual curves show significant differences between the levels of debonding observed for nominally identical bearings subjected to nominally identical loads and cyclic deformations. Part of this variation may be attributed to differences between manufacturers, but the relative ranking of bearings from the four manufacturers is different in almost every test and no one manufacturer proved consistently superior. This considerable scatter that exists in the debonding history of nominally identical bearings from different manufacturers suggests that the apparent random distribution of microscopic flaws, at which debonding starts, is at least as important as any consistent difference in quality among the four manufacturers.

Figure D-16 shows the internal effects of debonding in its early stage, wherein rubber of the side cover layer has separated from the edge of the steel shim. On rare occasions, this debonding extended into a shear crack that propagated as delamination back into the rubber layer as shown in Figure D-22. This latter cracking only occurred for tests with 6/8 θ_0 rotation, and only when the test was left running long after 100% surface debonding. Its presence could be detected only by cutting open the bearing. This was not done in all cases because it destroyed the bearing and prevented further testing at a later date, should that have proved desirable.

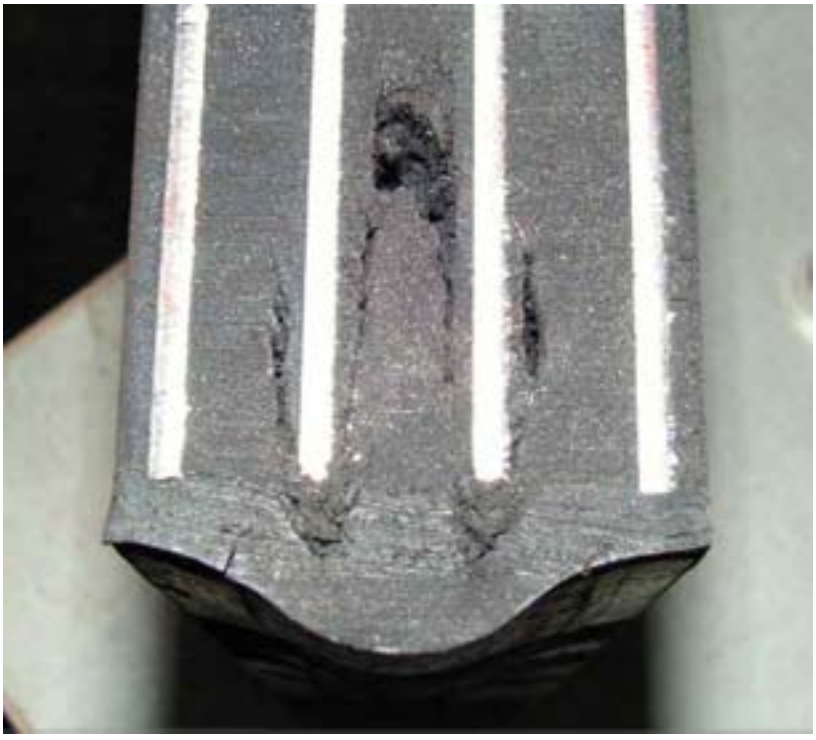

Figure D-22. Internal Damage Caused by Continuing Severe Cycling, Batch A1 Bearing

D.2.2.2 Comparisons among Manufacturers

The five tests in Figure D-17 through Figure D-21 show all of the bearings used for comparison among manufacturers. These included batches A2, B1, C1, and D1. Batch A1 was omitted from this comparison, because it had sharp corners on the shim edges, and this was observed to have a detrimental effect on bearing performance. The bearings provided by all manufacturers followed the same general trends in each test, but quantitative differences between the manufacturers are apparent. These differences were analyzed to assess the variability expected in normal bearing manufacturing practice.

In order to compare between manufacturers, common debonding levels were chosen at which the numbers of cycles required to reach that level could then be compared. Since bearings frequently had early initial debonding in weak spots and also strong spots that held together and did not debond, even after a large number of cycles, the three common levels were chosen to be mid-range levels, namely 25, 50, and 75% debonding. These damage levels were typically not directly measured during the test, and they are based upon interpolation between actual measured points. Table D-10 provides this comparison. The numbers in the table represent the number of cycles required to reach the given level of debonding.

Table D-10. CYC Series Interpolated % Debonded Values.

	% Deb.	A2	B1	C1	D1	Mean	COV
CYC5	25	337	450	56	95	235	81.0%
	50	531	652	156	354	423	51.0%
	75	1189	1703	1645	733	1317	34.4%
CYC7	25	907	1692	883	705	1047	42.0%
	50	1572	2989	3152	1613	2332	36.7%
	75	2856	8541	19037	4262	8674	84.4%
CYC9	25	104	217	6	96	106	81.9%
	50	248	398	18	192	214	73.3%
	75	973	1261	68	574	719	72.0%
CYC11	25	160	378	44	395	244	70.1%
	50	320	784	408	1396	727	67.3%
	75	633	1909	1736	3741	2005	64.2%
CYC12	25	3927	43956	8557	17117	18389	97.3%
	50	19599	62936	45749	191724	80002	95.7%
	75	36629	N/A	N/A	N/A	N/A	N/A

Table D-10 displays considerable scatter in the data, which appears to be greatest at lower load and rotation levels. (For example, tests CYC-7 and CYC-12 used the least punishing combinations of load and rotation, and had the largest coefficients of variation of cycle counts among manufacturers). The one clear conclusion that can be drawn is that there was so much overlap between manufacturers that individual bearing quality varied more than batch quality. Thus, it is unreasonable to rank any manufacturer as better or worse than any other. Any design method based on these tests should be keyed to the average performance, and not that of a particular manufacturer.

D.2.2.3 Effects of Magnitude of Rotation and Axial Stress Level

To find a correlation between the magnitude of rotation and the number of cycles, tests in which all variables except rotation were held constant were compared in greater detail. Tests CYC-5 and CYC-7 (5/8 P_0 axial load) and tests CYC-9, CYC-11, and CYC-12 (7/8 P_0 axial load) are compared in Figure D-23 through Figure D-26. These figures show all five standard tests for the four standard bearing batches. The data are the same as in Figure D-17 through Figure D-21, but they are re-arranged so that each plot is devoted to a single bearing source, and a logarithmic scale has been used for the cycle count.

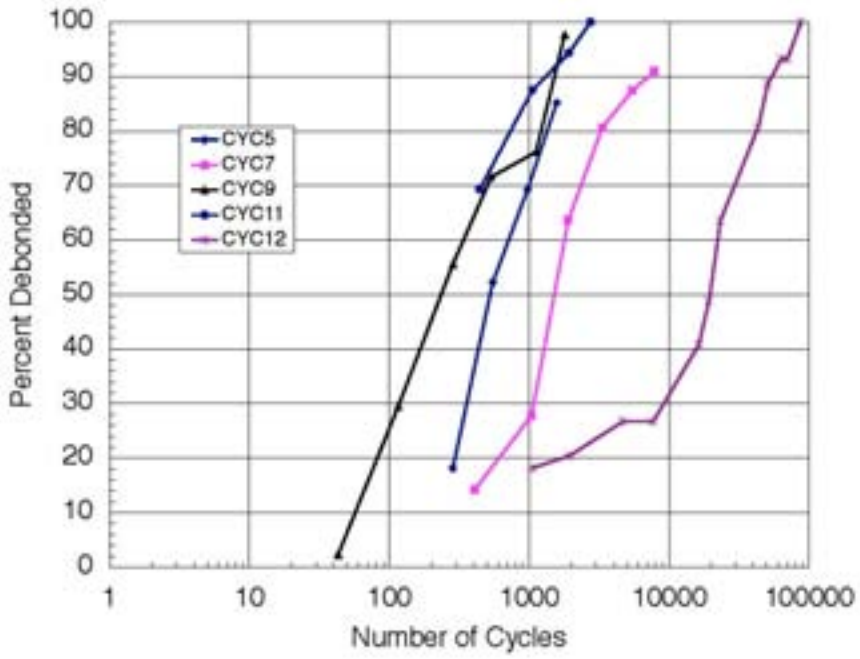

Figure D-23. Debonding for Type A2 Bearings: All CYC Tests

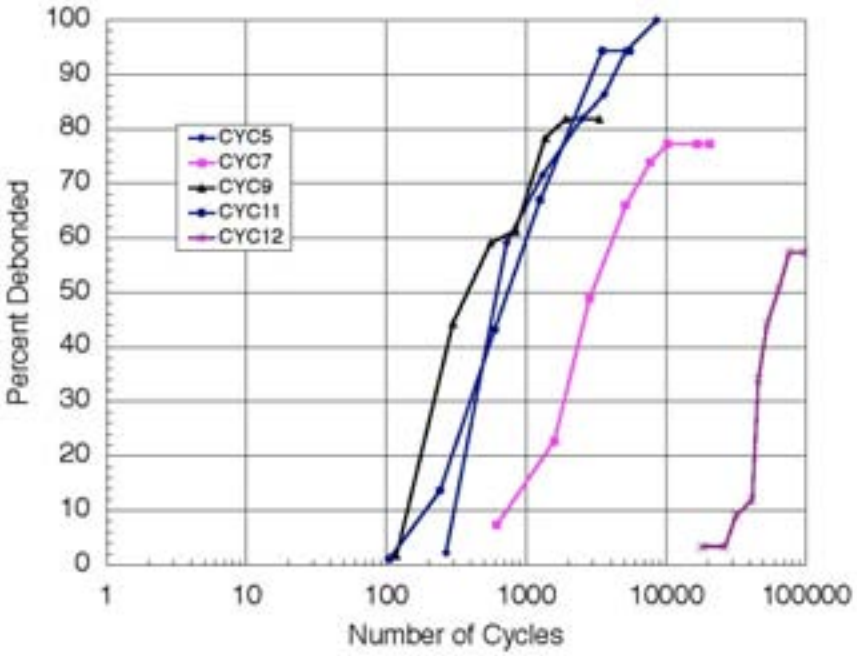

Figure D-24. Debonding for Type B1 Bearings: All CYC Tests

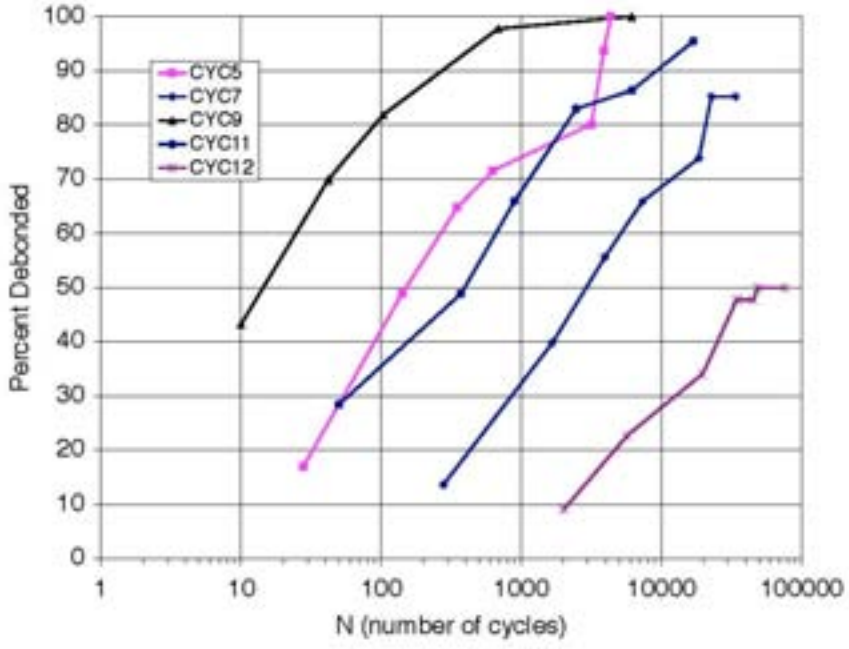

Figure D-25. Debonding for Type C1 Bearings: All CYC Tests

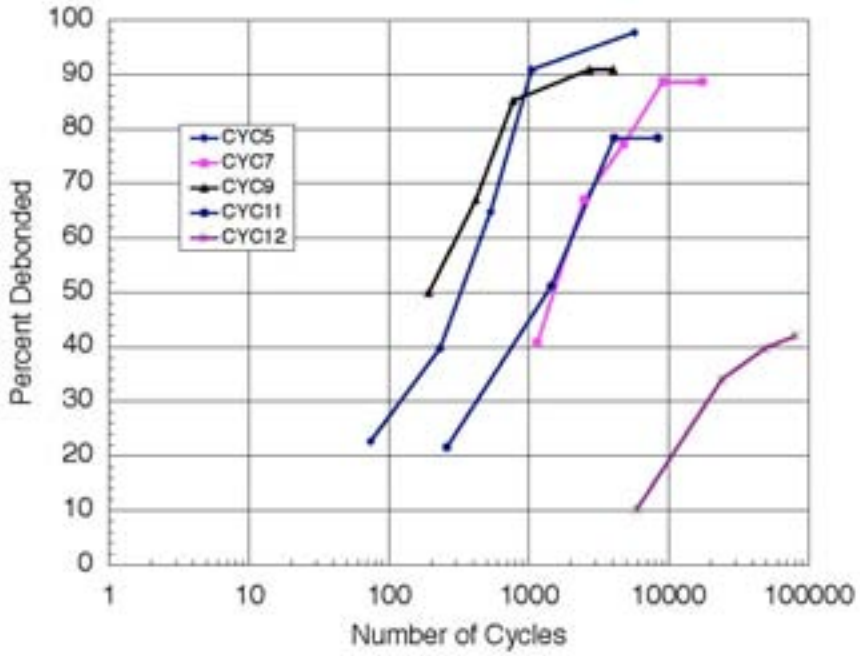

Figure D-26. Debonding for Type D1 Bearings: All CYC Tests

The results follow the expected pattern of faster damage accumulation with higher axial loads and larger rotations. With only one exception, the ranking of test severity was that CYC-9 led to the fastest damage accumulation, followed by CYC 5, 11, 7 and 12 in that order. The one exception was that for bearings A2, CYC-11 caused faster damage than CYC 5. Thus, for example, of the tests with $7/8P_0$ axial load (CYC-9, 11 and 12), larger rotation caused faster (or at least equal) damage accumulation in every case, and, for the bearings with equal rotations (CYC-7 and 11, CYC-5 and 9) larger axial load caused faster damage accumulation. These trends are rational, and also show that the differences between the loading demands were greater than the random differences in bearing resistance to debonding. The relative significance of axial load and rotation can be judged by comparing the results for CYC-11 ($7/8P_0$, $4/8\theta_0$) with CYC-5 ($5/8P_0$, $6/8\theta_0$). For bearings B1 and C1, those tests proved essentially identical in damage capability, while for bearings A2, CYC-11 proved the more severe and for bearings D1 the opposite was true. Thus, on average, tests CYC 5 and 11 had approximately equal damage capability.

In view of these trends, which were both consistent and independent of the bearing source, the results for each test were averaged across the four manufacturers. Because individual debonding readings were taken at different damage levels in each test, standard debonding levels had to be used for the averaging process. They were taken as 25%, 50% and 75%, and were obtained from individual results by interpolation. Those data are plotted in Figure D-27 and Figure D-28 for axial loads of $5/8P_{0\ and}$ $5/8P_0$ respectively. The data are shown as a mean (dashed line) ± 1 standard deviation (solid lines). Comparison of these curves shows that the curves can reasonably be approximated by straight lines with similar slopes or rates of deterioration in the semi-log scale. Thus it is likely that a curve based on a logarithmic fit would provide a good approximation. A more detailed effort to fit this data is in Appendix F.

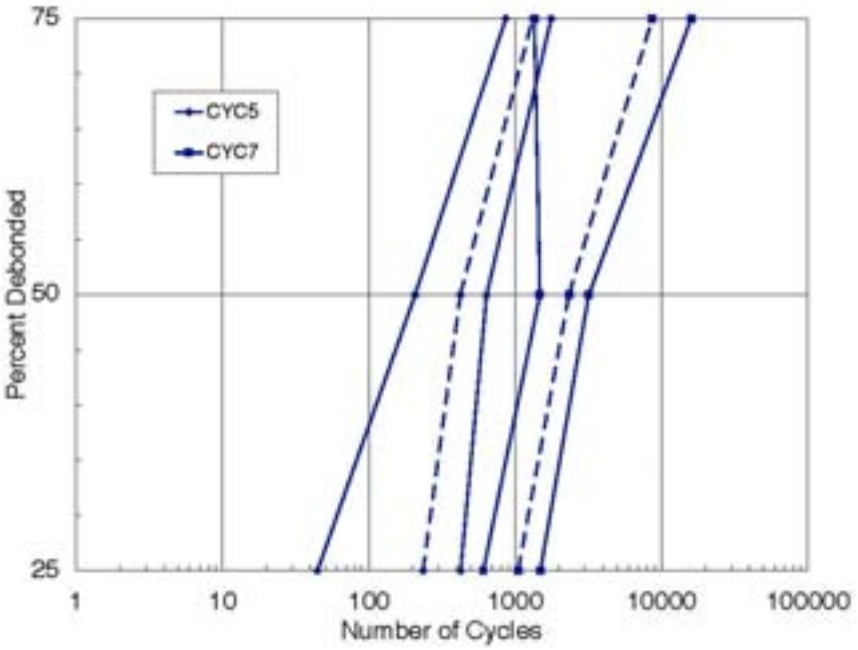

Figure D-27. Mean ±1 Standard Deviation for Debonding Curves, P=5/8 P0

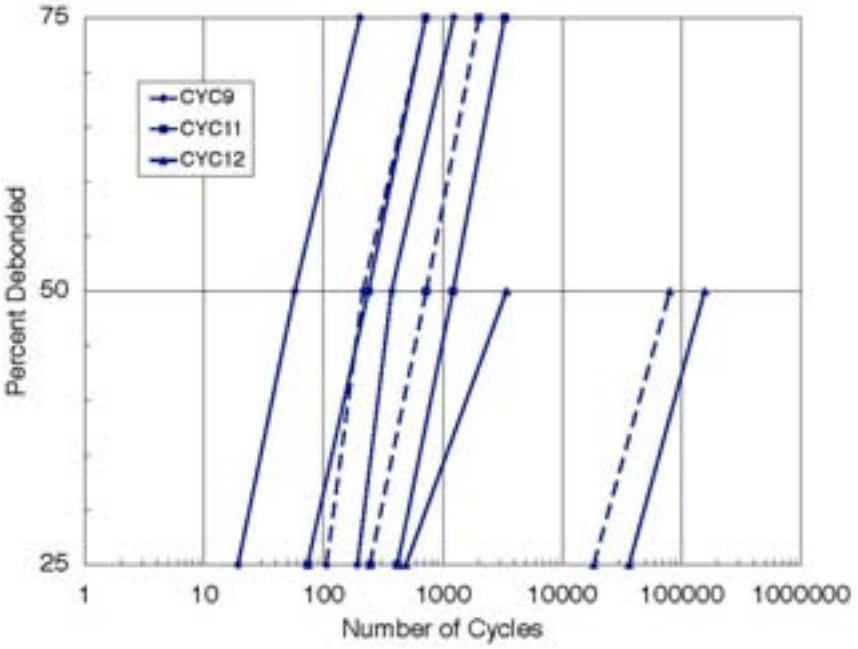

Figure D-28. Mean ±1 Standard Deviation for Debonding Curves, P=7/8 P0

As a further investigation of potential design criteria, the ratios of cycles to reach 50% debonding were compared in Table D-11. Data with axial loads of $5/8P_0$ (CYC 5, 7 and 8) and $7/8P_0$ (CYC-9, 11 and 12) are grouped separately. Within each group, the number of cycles needed to reach 50% debonding was normalized with respect to the number in the most damaging test (CYC-5 or CYC-9). The 50% debonding level was selected because it lay in the middle of the range and so was relatively free from scatter, and because it represents a level of relatively serious damage. After the high and low values were removed to create an adjusted mean, it appears that the $4/8\theta_0$ tests lasted about four times as long as the $6/8\theta_0$ tests and the $2/8\theta_0$ tests lasted four hundred times as long.

Table D-11. Cycle Count Ratios at 50% Debonding in Relation to CYC-5 and CYC-9

Batch	CYC5	CYC7	CYC8	CYC9	CYC11	CYC12
A1	1	7.8	15.0	1	2.0	8.0
A2	1	3.0		1	1.3	78.9
B1	1	4.6		1	2.0	158.2
C1	1	20.2		1	22.4	2517.8
D1	1	4.6		1	7.3	998.6
Mean		8.0			7.0	752.3
Adjusted Mean		5.6			3.7	412
COV (%)		32.8			81.8	123.7

Table D-11 also shows that reducing the axial load for $^1/_2\ \theta_0$ rotation has nearly twice the effect of reducing the axial load for $^3/_4\ \theta_0$ rotation. This supports a strain summation approach because the same axial stress should have a more significant effect on overall behavior when less rotation is applied.

D.2.2.4 Shim Edge Treatment

Batch A1 bearings had relatively sharp, machined edges and in most cases debonded faster than bearings from the other batches. For this reason, they were excluded from most of the comparisons. To evaluate quantitatively the effect of the sharp edges, a second batch, Batch A2, was ordered from manufacturer A to be identical to the Batch A1 bearings except with de-burred shims. Comparison of the A1 and A2 test results permits evaluation of this edge effect. Table D-12 shows results for Batch A1 and A2 bearings at different debonding levels. Batch A2 bearings performed better than batch A1 in each test, averaging 2.8 times longer to reach each debonding milestone, after high and low values were discarded. As a result of this finding, test series PLT was added to the test matrix to further investigate the influence of shim edge treatment.

Table D-12. Cycles to Reach Debonding Milestones for Shim Treatment Comparison

Test	25% Debonding			50% Debonding			75% Debonding		
	A1	A2	A2/A1	A1	A2	A2/A1	A1	A2	A2/A1
CYC5	72	337	4.7	143	531	3.7	308	1189	3.9
CYC7	591	907	1.5	1112	1572	1.4	1939	2856	1.5
CYC9	60	104	1.7	124	248	2.0	208	973	4.7
CYC11	127	160	1.3	245	320	1.3	363	633	1.7
CYC12	0	3927	∞	994	19599	19.7	2469	36629	14.8
Average			2.64			2.38			3.43
COV (%)			9.06			15.7			44.2

D.2.2.5 Long Term Test

As the design method in Appendix F was being developed, it became apparent that it would be very difficult to extrapolate the curves out far enough to reasonably predict the allowable rotations at the design life of a bridge. Over a 50-year life, a busy freeway bridge can expect about 50 million loaded trucks on the most heavily loaded (inside) lane (see Section F3.1 of Appendix F). Testing a bearing for this many cycles would take nearly a year, and was not possible within the time available for the research. However, it was decided that a test to 2 million cycles, which could be completed in two-weeks, would be beneficial.

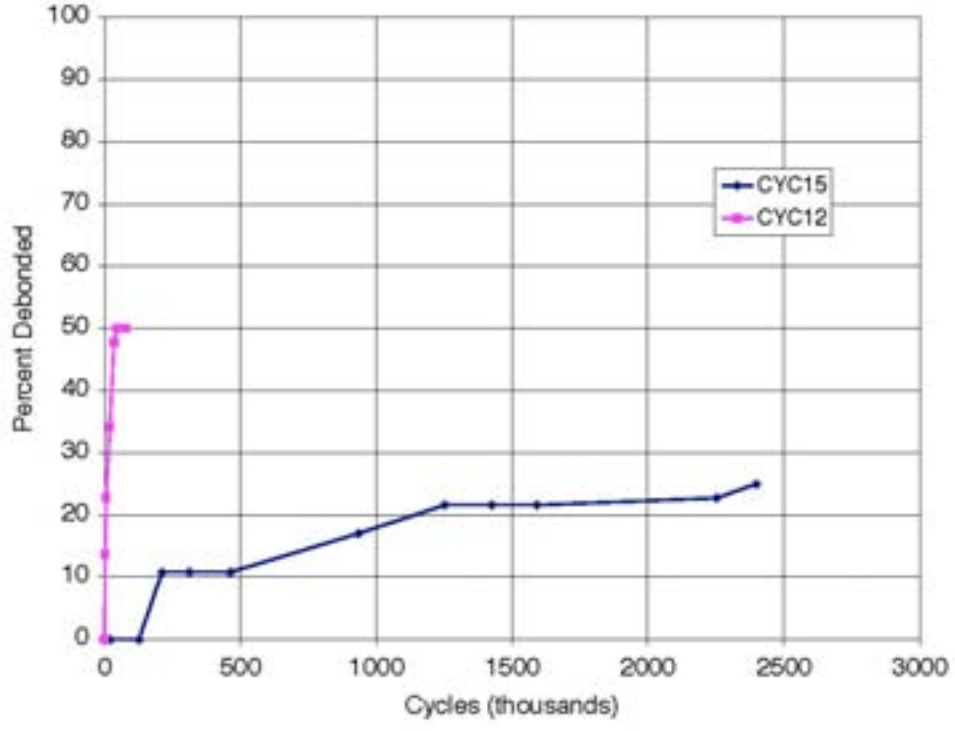

Figure D-29. Debonding for Long Term Test CYC-15_C1 and Comparison with CYC-12_C1

The magnitude of the rotations expected in the field is discussed in Section F3.3.1 of Appendix F. There it is shown that the largest girder end rotation, for any distribution of wheel or distributed loads consistent with a mid-span deflection of L/800, is 0.004 radians. For the long-term test, this rotation was rounded up to 0.005 radians. Due to time constraints, only one test (CYC-15) was performed, on a bearing from Batch C-1. The progression of debonding is plotted in Figure D-29, and results for test CYC-12 are shown for comparison, because that test extended to the second largest number of cycles. CYC-15 did not quite reach even the first standard debonding milestone of 25%. The significance of this test will be discussed in Appendix F.

D.2.2.6 Offset Rotation

Bridge bearings are unlikely to experience zero rotation under full dead load, so the cyclic live load rotations will probably be applied about a constant, non-zero, mean. This constant "offset" rotation might be caused by construction misalignment, unexpected permanent camber due to shrinkage and creep, dead load, etc. Tests CYC-13 and CYC-14 were designed to evaluate the influence of an offset rotation. That is, the tests examined whether, for a given cyclic rotation amplitude, the presence of a fixed offset rotation accelerated debonding.

Comparison with other constant amplitude-zero offset tests was made possible by choosing the total rotation (fixed offset plus cyclic rotation) to be equal to the total rotation of another test. For example, the 0.02 radians fixed rotation plus a 0.005-radian cyclic rotation in CYC-13 was equal to the total 0.025 radians rotation (in that case all cyclic) of test CYC-7. The offset tests were conducted on batch A1 bearings before the influence of the sharply milled shim edges became apparent. Therefore the absolute number of cycles that they sustained in reaching a given debonding level is smaller than for other bearings with de-burred edges, but, because all the tests compared in Figure D-30 and Figure D-31 were performed on A1 bearings, comparison of the test results provides a relative measure of the offset rotation effect. Figure D-30 shows tests CYC-7 and CYC-13, both of which had an axial load of $5/8P_0$ and a total rotation of 0.025 radians. Specimen CYC-13-A1, in which the rotation consisted of 0.020 offset plus 0.005 radians cyclic rotation, sustained many, many more cycles than specimen CYC-7-A1, in which the rotation was 0.025 radians (all cyclic). Specimen CYC-15-C1 is also shown, with $7/8P_0$ axial load, no offset and 0.005 radians cyclic rotation. The response of CYC-13 is much closer to CYC-15 than to CYC-7. The conditions in those two tests differed in three respects, two of which favored CYC-15: shim edge treatment (CYC-15 was de-burred, CYC-13 was sharp), offset rotation (CYC-15 had none, CYC-13 had 0.02 radians) and axial load (CYC-15 had $7/8P_0$, CYC-13 had $5/8P_0$). This result suggests that the offset rotation has much less effect on debonding than does cyclic rotation. This finding is similar to the behavior of metal in fatigue, in which the stress range is much more important than the peak stress or mean stress.

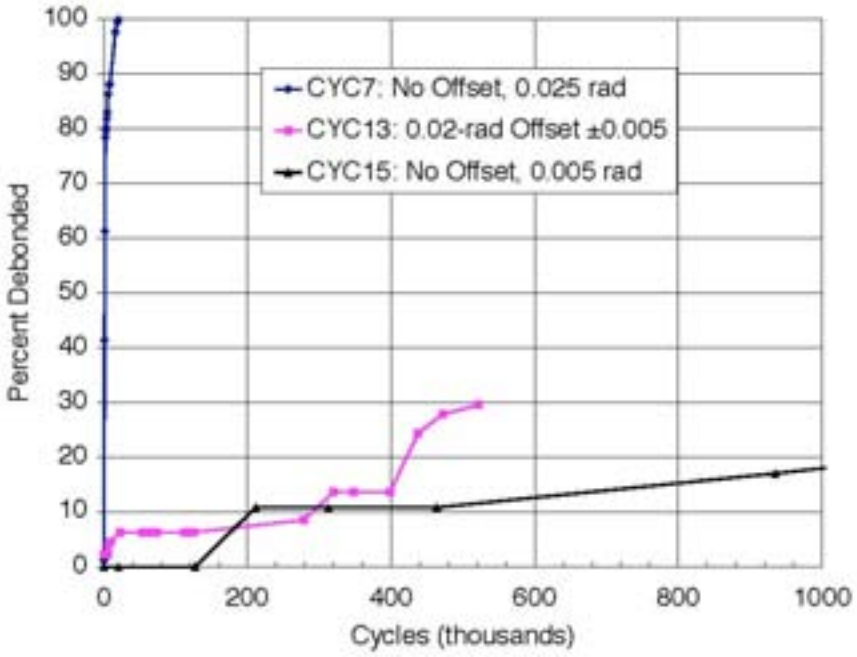

Figure D-30. Influence of Offset Rotation: Test CYC-7-A1 and Test CYC-13-A1

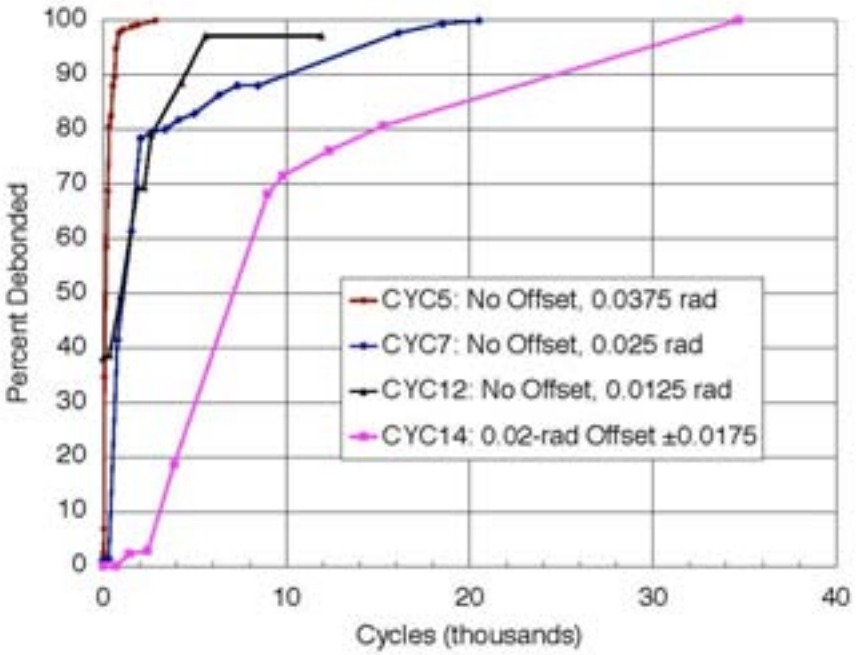

Figure D-31. Offset Rotation: Tests CYC-7-A1, CYC-7-A1, CYC-12-A1, and CYC-14-A1

In Figure D-31, comparison of CYC14 (θ = 0.02 ±0.0175) and CYC5 (θ = ±0.0375) shows that the latter inflicted damage much faster, despite the fact that both specimens had the same axial load and peak rotation. This finding is in agreement with that of CYC13, discussed above. No test was run with $^5/_8P_0$ and θ = ±0.0175 rad, so deducing directly the effect of the fixed offset rotation is not possible. However CYC7-A1 used $^5/_8P_0$ and ±0.025 rad, and so represents conditions that are quite close. It debonded significantly faster than CYC14-A1, suggesting that the additional cyclic rotation of ±0.0075 rad in CYC7-A1 was more damaging than the additional static ±0.02 radians of rotation in CYC14-A1. CYC12-A1 ($^7/_8P_0$, ±0.0125 rad) can be used for a further comparison. Its cyclic rotation was smaller than the 0.0175 of CYC14-A1, but its axial load was higher. It debonded at approximately the same rate as CYC7-A1 (i.e. faster than CYC14-A1) up until 80% debonding. The influence of the higher axial load was therefore greater than the benefit of the lower cyclic rotation angle.

Figure D-31 also compares CYC12 to CYC14. CYC12 had a smaller absolute cyclic rotation than CYC14 but debonded sooner, which was unexpected. Variability in the bearings may have caused some of this discrepancy, but, taken at face value, this result implies that a cyclic rotation added on top of an offset actually decreases the amount of damage expected. While this may appear illogical at first glance, there may be some logic demonstrated in this behavior. Cyclic rotation with an offset may inhibit complete reversal of the strains in the elastomer, which may cause less rapid crack growth (Cadwell et al. 1940). However, this benefit should not be relied upon to reduce damage, because the offset rotation is likely to be unreliable if it arises from construction misalignments. Furthermore, it must have an upper bound, after which the offset promotes, rather than inhibits, debonding. This can be seen by considering the case when the offset plus the cyclic rotation reaches the value at which debonding starts under monotonic rotation.

The main conclusion from these observations is that the addition of a static rotation is much less damaging than the addition of a significantly smaller cyclic rotation with many cycles of loading. The amplitude of the cyclic rotation should be the primary consideration in elastomeric bearing design.

D.2.3 SHR Test Series

The superposition of strains caused by compression, rotation and shear is important in elastomeric bearing design. The SHR Test Series was used to evaluate the effect of adding constant shear deformation to previously tested combinations of static axial load and monotonic or cyclic rotation. The SHR tests were performed at approximately 30% shear strain (0.5 inches shear displacement over the total rubber thickness of 1.5 inches) for most specimens, since this is representative of shear strains experienced in practice. However, a larger shear deformation was applied to Specimens SHR1 (test with 50% shear and a monotonically increasing rotation) and SHR-2 (test with cyclic rotation and 70% shear deformation). Table D-13summarizes the SHR Test matrix.

Table D-13. SHR Test Matrix

Name	No.	Manufacturer/ Batch	Plan Dimensions	Aspect Ratio	Shape Factor	Material	Axial Stress	Static Rotation	Cyclic Rotation	Shear Disp.
SHR	1	B1	9 x 22	2.44	6	CR50	4.0 GS	vary to 8%		50%
SHR	2	B1	9 x 22	2.44	6	CR50	7/8 P_0		4/8 θ_0	70%
SHR	3	B1	9 x 22	2.44	6	CR50	7/8 P_0		4/8 θ_0	30%
SHR	4	B1	9 x 22	2.44	6	CR50	5/8 P_0		6/8 θ_0	30%
SHR	5	B1	9 x 22	2.44	6	CR50	7/8 P_0		6/8 θ_0	30%
SHR	6	A2	9 x 22	2.44	6	CR50	7/8 P_0		2/8 θ_0	30%

Specimen SHR-1 was loaded with a 50% shear deformation, 7/8P_0 compressive stress, and a monotonically increasing rotation. This specimen is comparable to Specimen PMI-5-B1 except for the addition of the shear deformation. Specimen SHR-1 debonded at a smaller rotation than PMI-5-B1, and this shows that the shear had a limited adverse effect. However, the debonding for SHR-1 was only one inch occurring at -0.01 radians rotation (i.e. after reaching the positive peak with no damage and then passing through zero rotation), and it did not propagate any further. Specimen PMI-5-B1 did not show any debonding until complete reversal to -0.08 radians rotation after initial rotation to +0.08 radians. The somewhat earlier debonding in SHR-1 may therefore indicate one small weak spot on the bearing, rather than early damage because of the additional shear deformation.

Specimen SHR2 was loaded with a 70% shear strain and $^{7}/_{8}P_0$ axial load, and it was planned to be subjected to cyclic rotations. However, it was stopped prematurely because one of the compression diagonal bars described in Section C.4 failed. As a result, this specimen is not discussed further.

Specimens SHR-3 through SHR-6 provide the most useful information from the SHR Test Series. These results are compared in Figure D-32, Figure D-33 and Table D-13. Figure D-32 compares the debonding rate for Specimens CYC-9-B1 and SHR-5-B1, which were subjected to identical loading except that SHR-5-B1 also had a 30% shear deformation. The figure shows that the added shear increased the rate of bearing damage, but the increase was smaller than noted for many other factors in this research program. Figure D-33 compares the behavior of CYC-12-A2 and SHR-6-A2. This comparison shows that the addition of shear deformation extended the number of cycles needed to induce a given debond damage level in the bearing. This result was unexpected. Table D-13 summarizes the results for other tests, and shows the ratio of the number of cycles needed to reach the standard debonding milestones with and without shear. The value given is the average for the ratio at 25%, 50% and 75% debonding. A value greater than 1.0 implies that addition of shear deformations is damaging.

The evidence from these comparisons implies that the addition of constant shear strain has at most a small effect on the number of rotation cycles required to induce a specified amount of debonding damage. This may be explained by the fact that the magnitude of the average shear strain imposed on the rubber by the shear deformation is small compared to the nominal shear strains from axial load and rotation. For example, test CYC-11 has a shear strain from axial load of 1000% and a shear strain from rotation of 130%. A 30% additional shear strain imposed is only 3% of the total shear strain from the

test, so it follows that shear strains of this magnitude may be have only a very small impact, supporting the scattered evidence from the tests.

This conclusion must still be used with caution because prior research (Roeder, Stanton and Taylor, 1990) showed that cyclic shear deformations can be very damaging to elastomeric bearings. The conditions in the two studies were different, and that must be taken into account when evaluating the influence of shear deformations. The present study was conducted with constant shear deformation, whereas Roeder et al. applied some 20,000 cycles of 50% to 70% shear deformation. Shear deformations that large typically occur only on an annual basis, so the number of cycles is much smaller than the number of rotation cycles, which is governed by traffic loading. The shear deformations associated with day-to-night thermal cycles are clearly more numerous, but are also much smaller and therefore less damaging.

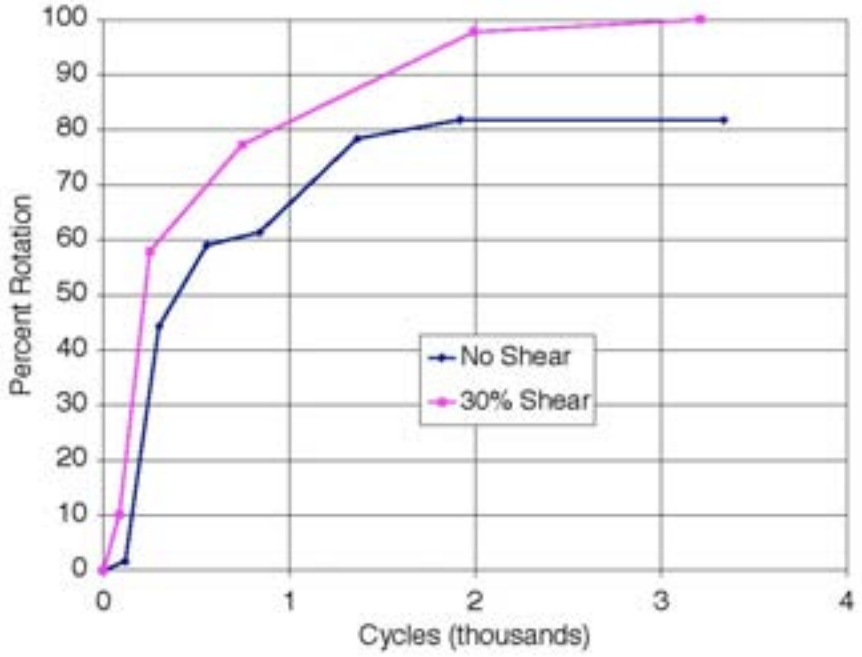

Figure D-32. Debonding Comparison for SHR-5-B1 and CYC-9-B1 Bearings

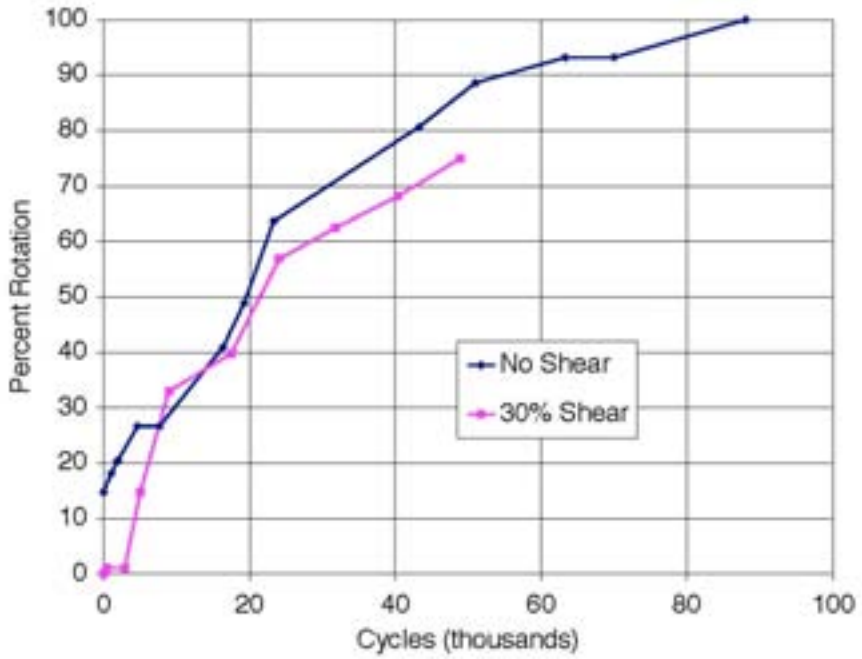

Figure D-33. Debonding for SHR-6-A2 and CYC-12-A2 Bearings

Table D-14. Cycles Needed to Initiate Debonding with 30% Constant Shear Added

CYC Test	SHR Test	$(N_{shear}/N_{cyc})_{ave}$
CYC11	SHR3	4.78
CYC5	SHR4	0.26
CYC9	SHR5	0.58
CYC12	SHR6	1.42

D.2.4 MAT Test Series

The MAT test series was developed to examine the effect on bearing performance of different material properties. The series included only three tests, as shown in Table D-15. The tests were designed to repeat three of the CYC series tests, but with specimens made from rubber with a nominal Shore A hardness of 60 durometer (Batch C2) rather than 50 (Batch C-1). Both batches were ordered from manufacturer C to minimize differences associated with different production processes. The loads used were the same as those in the corresponding CYC tests, without any change to reflect the different material properties. The MAT test specimens are compared to CYC-5, CYC-9 and CYC-11 from Batch C1, since these tests had identical compressive loads and cyclic deformation histories. Table D-16 summarizes the results. . Figure D-34 shows the rate of debonding for tests CYC-5-C1 and MAT-1-C2.

Table D-15. MAT Test Matrix

Name	No.	Manufacturer/ Batch	Plan Dimensions	Aspect Ratio	Shape Factor	Material	Axial Stress	Static Rotation	Cyclic Rotation	Shear Disp.
MAT	1	C2	9 x 22	2.44	6	CR60	5/8 P_o		6/8 θ_s	
MAT	2	C2	9 x 22	2.44	6	CR60	7/8 P_o		6/8 θ_s	
MAT	3	C2	9 x 22	2.44	6	CR60	7/8 P_o		4/8 θ_s	

Table D-16. Comparison of Cycles to Debonding with MAT Test Series

	MAT1/CYC5			MAT2/CYC9			MAT3/CYC11			
% Deb.	D50	D60	60/50	D50	D60	60/50	D50	D60	60/50	Avg.
25	56	282	5.0	6	209	36.0	44	999	22.7	21.2
50	156	793	5.1	18	486	26.7	408	6993	17.1	16.3
75	1645	3042	1.8	68	924	13.6	1736	33837	19.5	11.6
Average			4.0			25.4			19.8	16.4

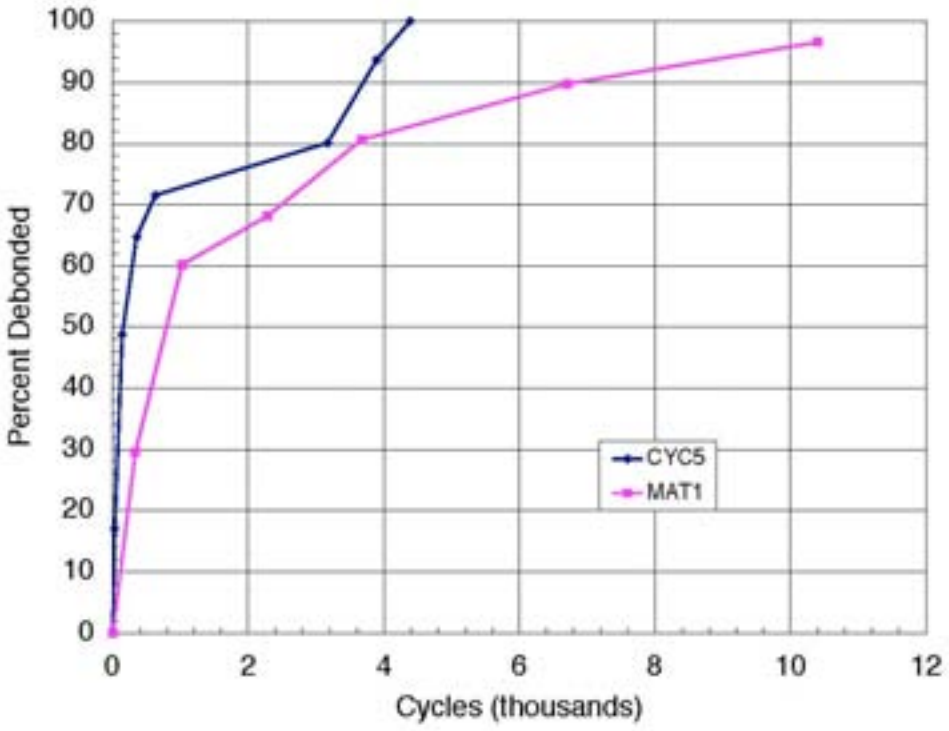

Figure D-34. Debonding Curves for CYC-5-C1 and MAT1-C2

Figure D-34 shows that MAT1 performed significantly better than CYC-5, debonding later at every point along the curve, and Table D-16 compares all three MAT tests with their corresponding CYC tests, and shows that they took up to 25 times the number of cycles to reach the 25%, 50% and 75% debonding milestones.

To evaluate this behavior, several points should be considered. First, a harder elastomer is likely to be better at resisting axial load because the resulting strains are smaller, but it may be less good at accommodating rotations, for which the strains are dictated by the girder rotation and are hardly influenced at all by the elastomer stiffness. Therefore the benefits of using a harder elastomer may depend on the relative magnitudes of the expected axial load and rotation. In test MAT-2, for example, the nominal shear strains due to axial load and rotation were 4.19 and 1.87, as opposed to 5.26 and 1.87 in the comparable test CYC-9-C1, for which the specimen was made by the same manufacturer but from 50 durometer material.

Second, it has historically been believed (see, e.g. BE1/76) that a higher elongation allows the elastomer to resist without failure or debonding a larger total shear strain demand. Since a harder elastomer will usually have a higher tensile strength but a lower elongation at break, the higher durometer material might be expected to perform worse.

Third, the axial loading on the CYC and MAT specimens was the same. An argument can be made that, to be truly comparable, each specimen should have had a load that was the same fraction of its nominal capacity, for example an average stress of cGS, where c is a dimensionless constant, G is the shear modulus and S is the shape factor. If that had been done, the MAT specimens would have had a higher axial load to reflect the higher G value. Because it was not done, the MAT specimens could be thought of as under-loaded, in which case their better performance is less surprising.

D.2.5 SHF Test Series

The SHF test series was designed to study the effect of shape factor on response, and the test matrix for the series is given in

Table D-17. These bearings were from Batch C2, so their hardness was 60 durometer and their shear modulus was approximately 144 psi, compared with the 115 psi for the 50 durometer materials used in Batch C1. Therefore, any comparisons with Batch C1 specimens should consider this difference.

Table D-17. SHF Test Matrix

Name	No.	Manufacturer/ Batch	Plan Dimensions	Aspect Ratio	Shape Factor	Material	Axial Stress	Static Rotation	Cyclic Rotation	Shear Disp.
SHF	1	C2	9 x 22	2.44	9	CR60	cyclic to 8000psi			
SHF	2	C2	9 x 22	2.44	12	CR60	cyclic to 8000psi			
SHF	3	C2	9 x 22	2.44	9	CR60	5/8 P_0		6/8 θ_0	
SHF	4	C2	9 x 22	2.44	9	CR60	7/8 P_0		6/8 θ_0	
SHF	5	C2	9 x 22	2.44	9	CR60	7/8 P_0		4/8 θ_0	
SHF	6	C2	9 x 22	2.44	12	CR60	5/8 P_0		6/8 θ_0	

The first tests, SHF1 and SHF2, were loaded with a cyclic axial load and so were similar to test PMI-1b. The virgin load-displacement curves from these tests are shown in Figure D-35 with the comparable curve for shape factor 6, 50 durometer (test PMI-1b-C1).

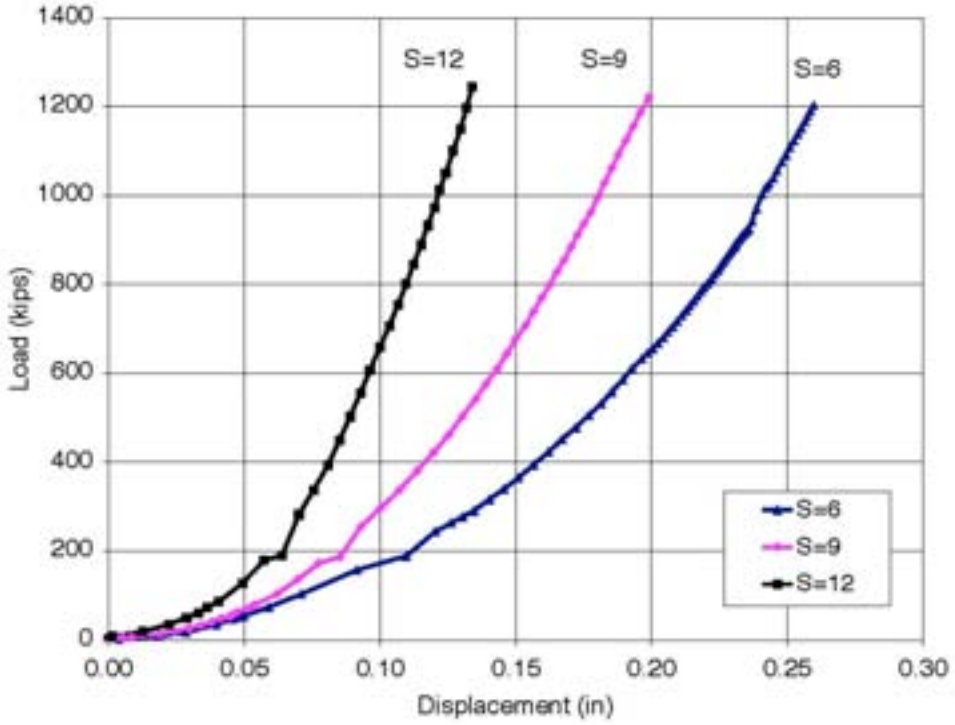

Figure D-35. Axial Load/Displacement Curves for Various Shape Factors

Figure D-35 shows the first-cycle curves for the three axial tests. Note that, at higher loads, the displacement of the shape factor 6 bearing is approximately twice that of the shape factor 12 bearing, with the shape factor 9 bearing midway between the two, implying an inverse linear relation between the shape factor and displacement.

No debonding occurred at all in the $S = 9$ and $S = 12$ bearings for these cyclic axial load tests, even though the $S = 12$ specimen was loaded to the machine capacity of 2400 kips, corresponding to 12 ksi axial stress. (The $S = 9$ specimen was loaded only to 1200 kips, or 6 ksi). The PMI-1b-C1 specimen showed slight debonding after 2 cycles, but the debonding did not propagate.

Tests SHF-3 through SHF-6 constitute the standard series of cyclic rotation tests, comparable to CYC-5, 9, 11, on bearings with shape factors of 9 and 12. The loads and rotations used for these tests were changed to account for higher S by calculating the maximum shear strains according to Stanton and Lund (2005), but the loads were not increased to account for the harder elastomer. In all cases the bearings with larger shape factors performed very well, and their performance is compared with that of specimens CYC-5 and CYC-9 in Table D-18. Because the CYC and SHF bearings had different shear moduli, the SHF bearings should be expected to sustain smaller damage levels. The table shows that the shape factor 9 bearings lasted 7 to 13 times longer, and shape factor 12 bearings lasted about 130 times longer, than the shape factor 6, 50 durometer, bearings subjected to the same load history. Test SHF 5 is not included in the table because the test showed no debonding after 20,000 cycles and the test was stopped so that other tests could be performed.

Table D-18. Number of Cycles to Debonding Milestones for Different Shape Factors

	CYC5/SHF3			CYC5/SHF6			CYC9/SHF4			
% Deb.	S=6	S=9	9/6	S=6	S=12	12/6	S=6	S=9	9/6	Avg.
25	282	2777	9.9	282	15611	55.4	209	1996	9.6	24.9
50	793	4995	6.3	793	151930	191.6	486	6753	13.9	70.6
75	3042	17796	5.8	3042	422112	138.7	924	14135	15.3	53.3
Average			7.3			128.6			12.9	49.6

D.2.6 ASR Test Series

The purpose of the ASR test series was to evaluate the effect of the aspect ratio of the bearing. Square bearings (i.e. aspect ratio of 1.0) were subjected to axial load (comparable to test PMI-1b) and combined axial load plus cyclic shear (comparable to tests CYC-5, 9 and 11). The ASR bearings were made from Batch C1 rubber, with a hardness of 60 and a shape factor of 6. To achieve the desired aspect ratio while keeping the shape factor the same, the layer thickness had to be 3/8", rather than the ½" used in he standard bearings. Table D-19 shows the test matrix for the ASR specimens.

Table D-19. ASR Test Matrix

Name	No.	Manufacturer/ Batch	Plan Dimensions	Aspect Ratio	Shape Factor	Material	Axial Stress	Static Rotation	Cyclic Rotation	Shear Disp.
ASR	1	C2	9 x 9	1	6	CR60	cyclic to 8000psi			
ASR	2	C2	9 x 9	1	6	CR60	5/8 P_o		6/8 θ_o	
ASR	3	C2	9 x 9	1	6	CR60	7/8 P_o		6/8 θ_o	
ASR	4	C2	9 x 9	1	6	CR60	7/8 P_o		4/8 θ_o	

The loading in test ASR-1, was the same as in test PMI-1b (cyclic axial test loaded to 8000 psi). The load-displacement curve is shown in Figure D-36, and is compared to that of a standard 9-inch by 22-inch bearing (aspect ratio =2.44), with both shape factor 6 and 60-durometer neoprene. Specimen ASR-1, with aspect ratio 1.0, is about twice as stiff as its counterpart with aspect ratio 2.44. Some of this difference must be attributed to the difference in G for the two bearings, but that only accounts for a factor of 1.25, leaving a further factor of 1.6 unexplained.

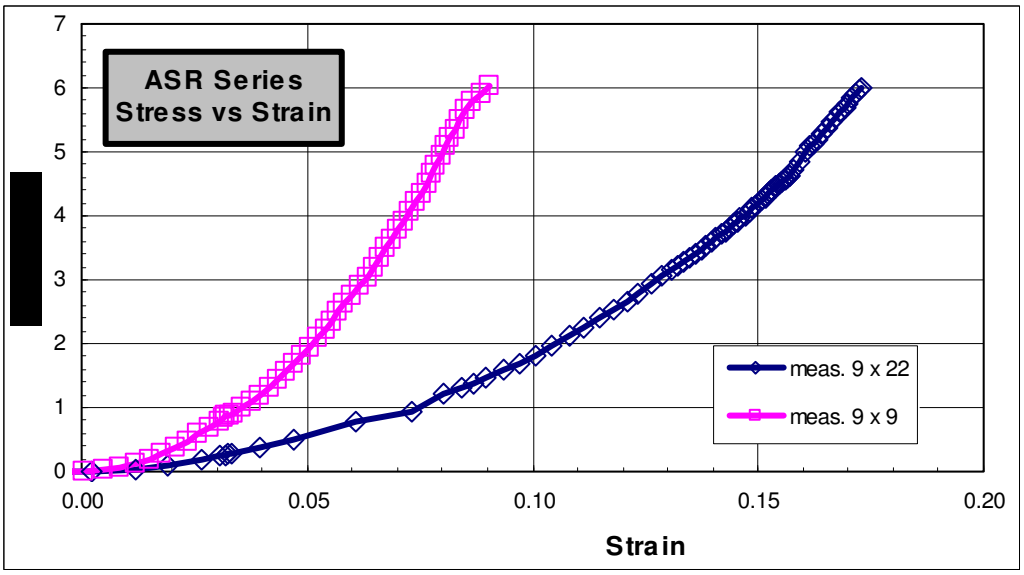

Figure D-36. Axial Load-Displacement Curves for Different Aspect Ratios

Tests ASR-2, ASR-3 and ASR-4 were designed to simulate the same compressive loads and cyclic rotational history as MAT-1 2 and 3, which were in turn the same as CYC-5, 9 and 11. Tests ASR2 and ASR4 both slipped sideways near the end of their runs and were abandoned before 75% debonding. Test ASR3 also had to be abandoned early so that the rotation rig could be repaired. Therefore, the data set is incomplete, as shown in Table D-20. However, the lower aspect ratio bearings showed consistently much better performance than the standard 22" by 9" bearings under the same loads.

Table D-20. Number of Cycles to Debonding Milestones for Different Aspect Ratios

	ASR2/MAT1			ASR3/MAT2			ASR4/MAT3			
%Deb.	AR2.4	AR1	1/2.4	AR2.4	AR1	1/2.4	AR2.4	AR1	1/2.4	Avg.
25	282	1232	4.4	209	2949	14.3	999	62389	62.4	25.6
50	793	4369	5.5	486	7188	14.7	6993	N/A	N/A	10.1
Average										

D.2.7 PLT Test Series

The PLT Series tests were designed to investigate the effects of shim edge treatment. The series consisted of two bearings with sharp-edged shims, two bearings with deburred shims, and two bearings with shim edges machined to a semicircular profile. Because this series was added late in the program in response to the discovery that the A1 bearings with their sharp-edged shims debonded prematurely, time was short, and only two load histories (the same as tests CYC-5 and CYC-9) could be used, Table D-21 shows the test matrix.

Table D-21. PLT Test Matrix

Name	No.	Manufacturer/ Batch	Plan Dimensions	Aspect Ratio	Shape Factor	Material	Axial Stress	Static Rotation	Cyclic Rotation	Shear Disp.
PLT	1	A3 - sharp shim	9 x 22	2.44	6	CR50	5/8 P_0		6/8 θ_0	
PLT	2	A3 - sharp shim	9 x 22	2.44	6	CR50	7/8 P_0		6/8 θ_0	
PLT	3	A3 - deburred	9 x 22	2.44	6	CR50	5/8 P_0		6/8 θ_0	
PLT	4	A3 - deburred	9 x 22	2.44	6	CR50	7/8 P_0		6/8 θ_0	
PLT	5	A3 - rounded	9 x 22	2.44	6	CR50	5/8 P_0		6/8 θ_0	
PLT	6	A3 - rounded	9 x 22	2.44	6	CR50	7/8 P_0		6/8 θ_0	

The debonding history is shown in Figure D-37 and Figure D-38. During the CYC series, the Batch A2 bearings with the deburred shims performed better than the A1 bearings with sharp-edged shims. The same behavior was also seen in The PLT test series, at both load levels. The bearings with machined shims (PLT-5 and 6) generally behaved the best of all, but the improvement gained by machining rather than de-burring was deemed to be not great enough to justify the considerable additional cost. De-burring can be done with a belt-sander, grinder, or special hand-tool, and is relatively fast and in expensive.

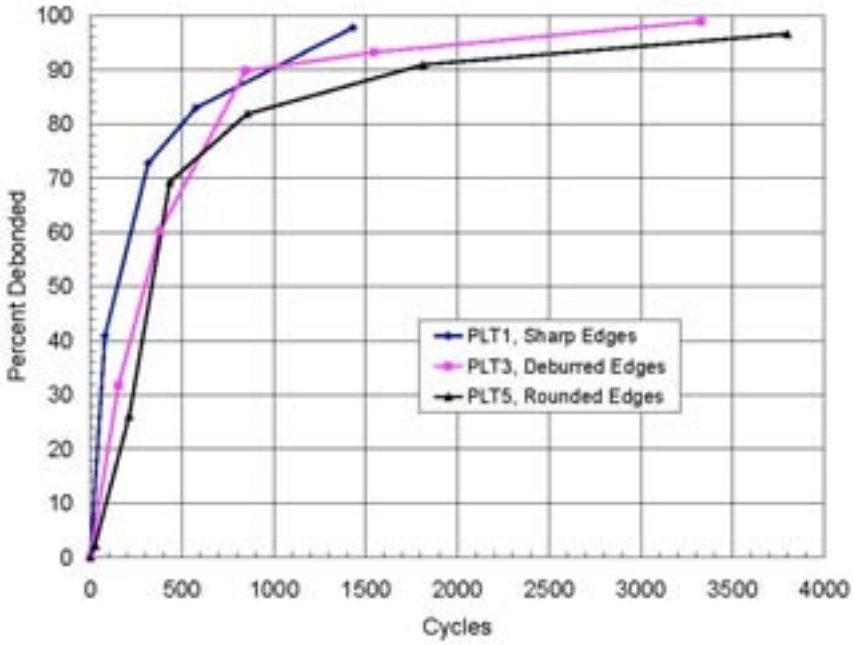

Figure D-37. PLT Test Series: Debonding with $^5/_8P_0$ Axial Load and $2/8\theta_0$ Rotation

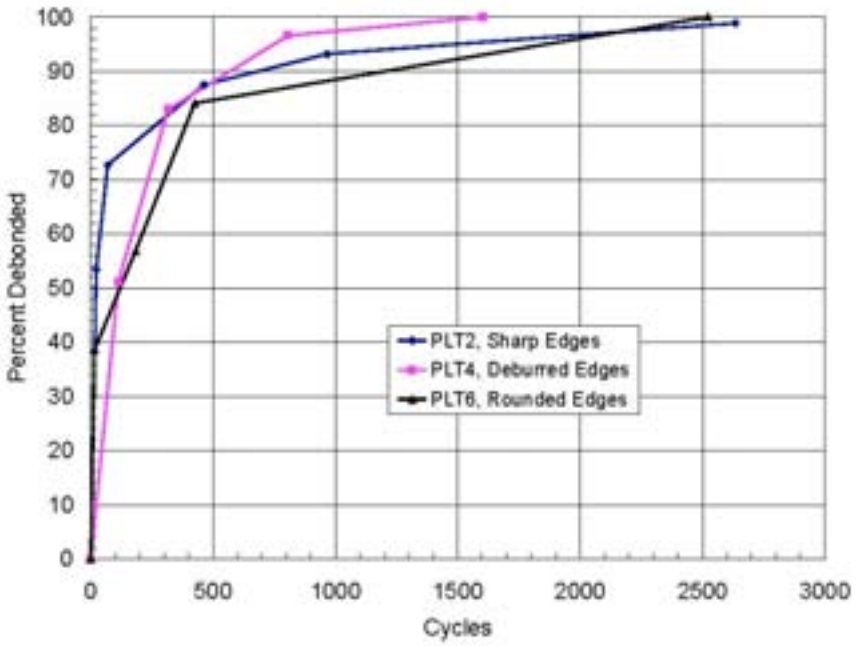

Figure D-38. PLT Test Series: Debonding with $^{7}/_{8}P_0$ Axial Load and $6/8\theta_0$ Rotation

These data are also presented in Table D-22 and Table D-23, where the numbers of cycles required to achieve debonding milestones of 25, 50, and 75% are presented. As seen in the average numbers, the deburred shims required 2 to 6 times as many cycles to achieve a given level of damage as the shims with sharp edges.

Table D-22. Tests PLT-1, 3, 5. Debonding vs. Cycle Number for Various Shim Edge Treatments

% Deb	PLT1	PLT3	PLT3/PLT1	PLT5	PLT5/PLT1
25	49	120	2.5	203	4.1
50	147	297	2.0	334	2.3
75	374	612	1.6	624	1.7
Average			2.0		2.7

Table D-23. Tests PLT-2, 4, 6. Debonding vs. Cycle Number for Various Shim Edge Treatments

% Deb	PLT2	PLT4	PLT4/PLT2	PLT6	PLT6/PLT2
25	10	55	5.5	10	1.0
50	21	110	5.2	120	5.7
75	130	265	2.0	344	2.6
Average			4.3		3.1

D.3 Supplemental Tests

Material property tests were conducted to evaluate the material properties, and diagnostic tests were used to determine the instantaneous state of damage in a bearing. These tests are summarized in this section.

For each batch of bearings received, the manufacturer conducted standard material property tests. The results were supplied to the researchers, and are summarized in

Table D-25. In addition, the researchers conducted their own shear modulus test and bulk modulus tests, which are described in Section D.3.1. These served not only as a check on the manufacturer's data, but also provided needed input for the Finite Element model, described in Appendix E.

A torsion test rig was specially designed and built to determine the instantaneous state of damage in the bearing, caused by cyclic loading in the Multi-load rig. It is described in Section D.3.2.

D.3.1 Material Property Tests

D.3.1.1 Material Tests by Manufacturers

The manufacturer of each individual bearing set performed elastomer material property tests, which are summarized in

Table D-25. That table shows that the elastomers used in all test bearings passed all of the tests, with the exception that no tear test results (ASTM D624) were provided with batches A2, B1, and C1, so their tear resistance is unknown.

Batch C2 bearings were used in the MAT, SHF, and ASR Test Series, and they behaved better than their C1 counterparts in these test series. This is surprising because, of the short-term physical properties that might be considered important for debonding (tensile strength, elongation at break, tear resistance and adhesion), the C2 properties were worse than the C1 properties in all cases but one (tensile strength). In particular, some specifications (e.g. BE1/76) have linked the total permissible shear strain in service to the elastomer's elongation at break, but comparison of the C1 and C2 results showed that, in this program, the better performance was provided by the material with the lower elongation.

The elongation at break and tensile strength are presented in Table D-24 with the other mechanical properties. They are also plotted as functions of hardness in Figure D-39 and Figure D-40 respectively. Considerable scatter exists in both quantities for the nominal 50 durometer materials. However, when the 60 durometer material is included, trends exist by which the tensile strength increases and the elongation decreases for harder elastomers. Such an inverse relationship between strength and elongation is common to many materials, including elastomers. Here the material with the second highest strength (C2) had the lowest elongation, and the one with the second highest elongation (A1) had the lowest strength. Batch B1 was unusual in that it had both the highest strength and elongation.

The four properties tensile strength, elongation at break, shear modulus G and bulk modulus K were measured. The values of E and ν were derived from G and K as explained in Section D.3.1.2.2.

Table D-24. Mechanical Properties of the Elastomers in Each Batch.

Batch	Durometer nominal (points)	Durometer measured (points)	Tensile strength (psi)	Elongation at break (%)	G measured (psi)	K measured (psi)	E derived (psi)	nu derived (-)
A1	50	51	2250	675	97.3	445300	291.9	0.49989
A2	50	52	2711	526	88.4	481800	265.2	0.49991
B1	50	51	2953	683	119.3	467200	357.9	0.49987
C1	50	48	2336	488	114.5	468300	343.5	0.49988
D1	50	52	2513	538	95.7	453100	287.1	0.49989
ave	50	50.8	2553	582	103.0	463140	309.1	0.49989
stdev	0	1.64	285.2	90.5	13.20	14234	39.59	1.42E-05
cov	0.000	0.032	0.112	0.155	0.128	0.031	0.128	0.000
C2	60	59	2871	428	143.5	485500	430.5	0.49985
$C2/ave_{50}$	1.20	1.16	1.12	0.74	1.39	1.05	1.39	1.00

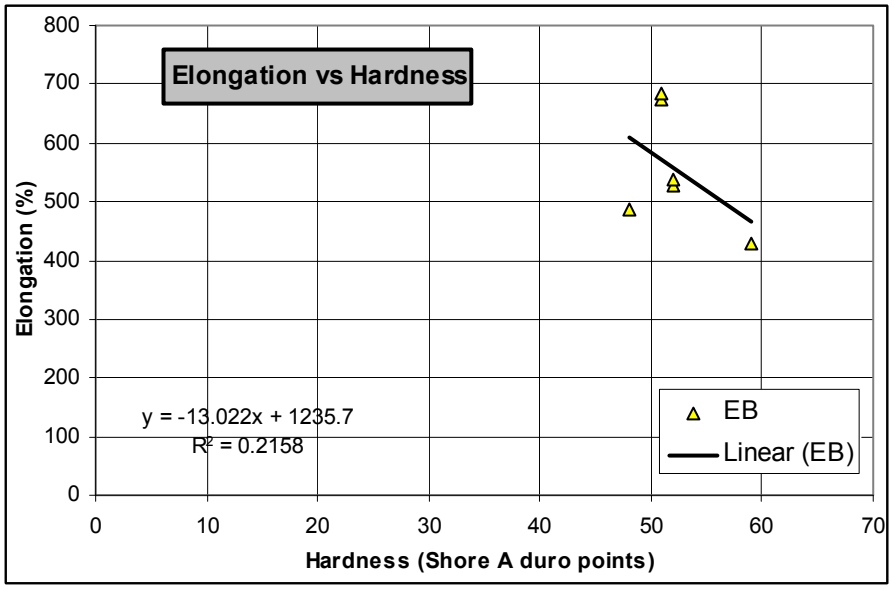

Figure D-39. Elongation at Break as a Function of Hardness.

Table D-25. Manufacturers AASHTO and Quality Control Tests

Test	ASTM	Required	A1	A2	B1	C1	C2	D1
Original Physicals								
Hardness (Shore A)	D2240	50±5 (C2:60±5)	51	52	51	48	59	52
Tensile Str. (psi)	D412	2250	2250	2711	2953	2336	2871	2513
Elongation (%)	D412	400	675	526	683	488	428	538
Heat Resistance (70hrs at 212°F). Max % change in:								
Hardness	D573	15	3	4	1	3	5	8
Tensile Strength	D573	-15	-11	-5	-5	-7	-2	-9
Elongation at Break	D573	-40	0	-13	-8	-9	-7	-1
Compression Set (22 hrs at 212°F)								
Max. %	D395(B)	35	22	17	21	21	26	17
Tear Resistance (min. lb/in)	D624	180	207	N/A	N/A	N/A	Pass	196
Ozone Resistance	D1149	No Cracks	Pass	Pass	Pass	Pass	Pass	Pass
Low Temperature								
Brittleness at 40 °F	D1149	No Cracks	Pass	Pass	Pass	Pass	Pass	Pass
Adhesion								
Bond (lb/in)	D429(B)	40	74	78	79.4	104	83	98
Instantaneous Thermal Stiffening								
Grade 3 at -40 °F, max. (ratio)	D1043	4	3.18	1.41	N/A	N/A	N/A	N/A
Proof Load	M251	1.5 design	Pass	Pass	Pass	Pass	Pass	Pass

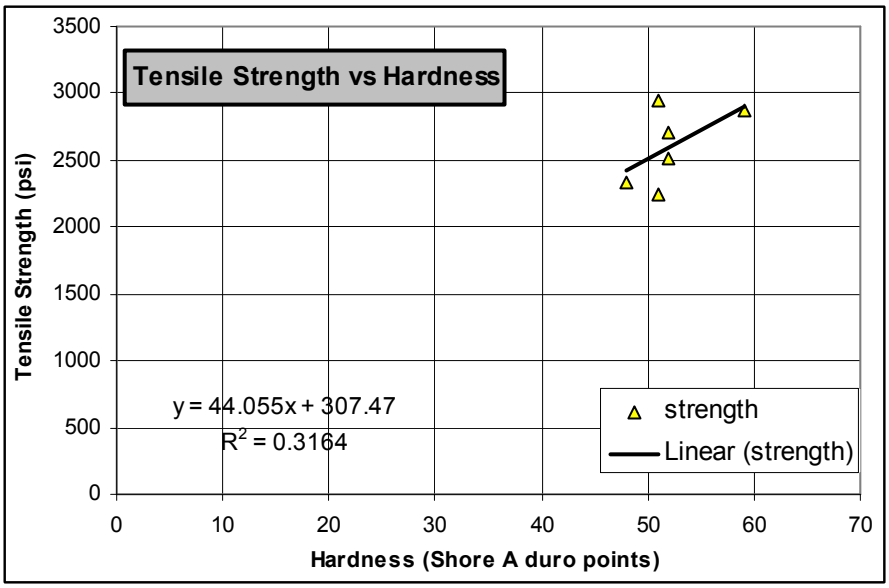

Figure D-40. Tensile Strength as a Function of Hardness.

Table D-26 shows the properties of the steel used in the elastomeric bearings. All rotation tests in this research were performed well within the elastic range of the shim plates. However, in the PMI tests with axial loads over 8000 psi, many of the steel plates yielded, and some fractured. However, these behaviors are predictable by current bearing design provisions.

Table D-26. Steel Plate Properties from Manufacturers

Batch	Yield (ksi)	Tensile (ksi)	% Elongation
A1	46.8	60.6	40
A2	56.6	70.7	32
B1	48	63	32
C1	43.2	62.6	26
C2	43.2	62.6	26
D1	39	55.3	42.5

D.3.1.2 Material Tests by the University of Washington

Shear modulus, *G,* and bulk modulus, *K,* tests were completed at the University of Washington for all six batches of bearings. The tests used specimens cut from the bearings themselves, and were prepared and conducted using the procedures outlined in Appendix C. The results of these tests are summarized in Table D-24. The values of *G* and *K* were measured, and *E* and ν were deduced from them.

D.3.1.2.1 Shear Modulus Tests

The shear modulus tests were completed in approximate accordance with ASTM D4014. The primary differences were:

- The load was not reduced to zero between cycles, because doing so would cause the specimen to fall out of the grips. Instead it was dropped to a standard value of 100 lbs.
- The peak load did not always correspond to 50% shear strain.

A typical shear force-displacement plot is shown in Figure D-41. Each sample exhibited softening behavior up to a shear strain between 50% and 75%, and then subsequent hardening behavior. ASTM D4014 specifies that *G* be taken as the secant stiffness between the data point and a point corresponding to a 25% greater shear strain. The first data point is to be taken at a load equal to 2% of the peak load during the conditioning cycles to 50% strain. Unfortunately this was not possible with the equipment available, for the reasons given above.

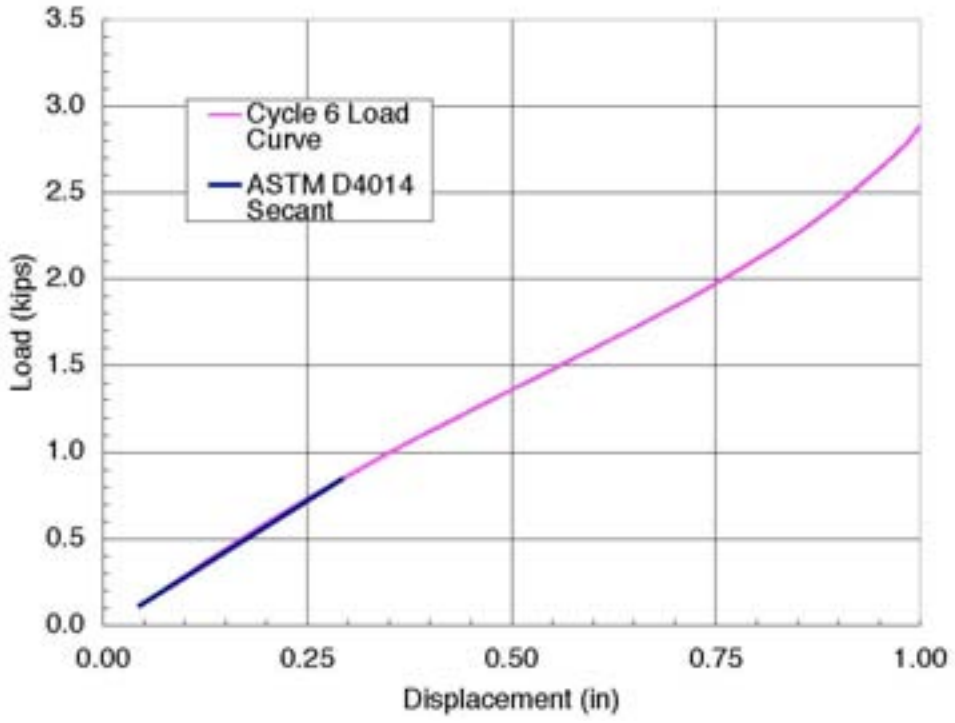

Figure D-41. Typical Load/Displacement Curve for Shear Modulus Test

ASTM D4014 allows a range of specimen dimensions. In particular, it is possible to use specimens with different length/thickness ratios, *L/t*, provided *L/t* > 4.0. Because the total displacement may be thought of as consisting of a bending and a shear component, the researchers suspected that different *L/t* ratios might lead to different *G* values for the same material, because the relative magnitudes of the components would depend on the L/t ratio. In order to investigate this issue, the specimens were first tested with *L* = 5" and *t* = 0.5", as shown in Figure C-17. Cuts were then made to reduce the lengths of the rubber blocks to 3", 2" and then 1.5", and the test was re-run at each length. As described in Section C.5, the minimum load on the specimen was controlled by the need to prevent the specimen from falling out of the grips. Because the same minimum load was used for all specimens, the stress, and therefore the shear strain, at the first data point was different for each length. Therefore any difference in modulus attributable to the specimen *L/t* ratio was masked by the effect of the initial curvature of the curve.

The investigation showed the following

- The effect of the specimen dimensions should be studied carefully and, if necessary, the permissible dimensional ratios such as *L/t* should be specified more precisely. If all specimens use identical, standard, dimensions, as is often done for specially prepared samples, this does not matter. However when a sample is cut from a finished bearing, the thickness is determined by the bearing layer thickness, dimensions different from the standard ones may result, and may lead to variations in the *G* value obtained. While cutting specimens from a finished bearing is not the norm, it is still an important case, because the reason for doing it may be to resolve a dispute. Then, having a reliable, unambiguous test procedure is very critical
- The value of G obtained from the test depends on where the first data point is taken. If the load on the specimen can be dropped right down to zero, this does not matter. However, for specimens cut from finished bearings, the dimensions of the test specimen may limit the choices for the minimum load. It would be helpful locate the minimum load higher up the curve, so that testing specimens cut from a finished bearing is feasible.

The shear moduli from Table D-24 are plotted as a function of hardness in Figure D-42. Although scatter exists among the 50 durometer materials, the trend of higher shear modulus for the harder elastomers is clear.

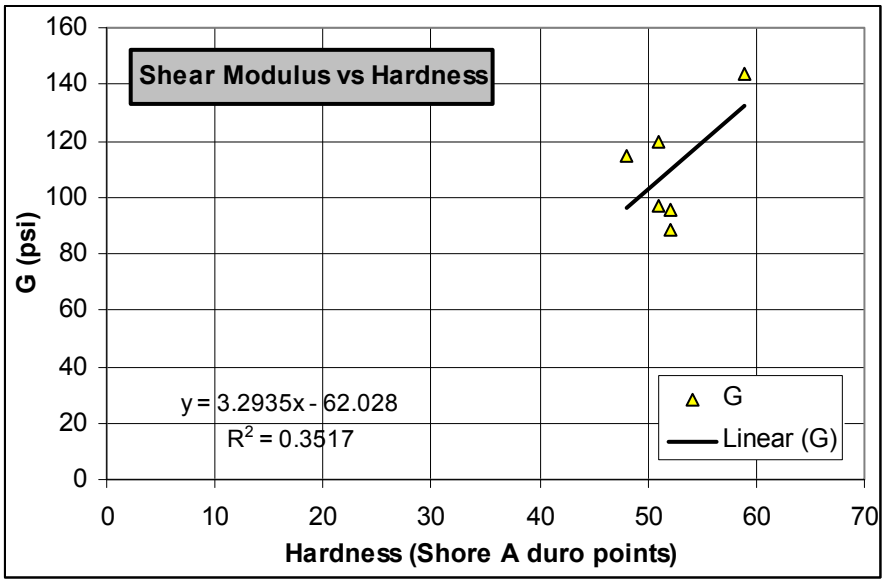

Figure D-42. Shear Modulus vs. Hardness.

D.3.1.2.2 Bulk Modulus tests

The bulk modulus tests were designed specifically for this research and not in accordance with any particular material test specification. The equipment used is described in Section C.6. These tests were performed to develop the material properties needed for the FE analyses described in Appendix E.

A typical load-displacement plot is shown in Figure D-43. Displacement occurred with little resistance up to the point when the elastomer filled all the voids in the test chamber. After this, the displacement was essentially linear with load. It was cycled five times to allow the response to stabilize.

The bulk modulus is based on a linear fit to the load displacement curve. Therefore, the secant stiffness was taken between two standard points (F_1, d_1) and (F_1, d_1), where $F_1 = 8$ kips and $F_2 = 28$ kips. For all tests, the absolute displacement varied because of the relatively arbitrary zero to the displacement, but the force-displacement relationship was consistently linear between these two points.

The bulk modulus is the ratio of the change in hydrostatic pressure to the volumetric strain of a material, so these two values had to be derived from the test data. The problem is complicated slightly by two features of the test. First, the steel shims were present in the sample, and they compress slightly, although much less than the rubber, under the axial stress. They were included to minimize any roughness on the top and bottom of the rubber discs that might have occurred if the rubber had been cut free of the steel. Second, the steel cylinder expands when the internal pressure is applied. When these two facts are taken into account, it can be shown that

$$K = \frac{k_{test} h_r}{\left(1 - \frac{k_{test}}{k_{shims}}\right)\left(1 - \frac{4h_r}{D}\frac{k_{test}}{k_{cyl}}\right)} \qquad \text{(D-1)}$$

where

k_{test} = stiffness measured in the test (ksi/inch) = $\Delta p/\Delta h$

k_{shims} = axial stiffness of steel shims = E_{steel}/h_{shims}

k_{cyl} = radial stiffness of cylinder (ksi/inch)

Δh = change in thickness of specimen (i.e. displacement)

Δp = change in stress on the specimen

h_r = total rubber thickness

D = internal diameter of cylinder

Equation (D-1) is based on the assumption that the state of stress in the rubber is hydrostatic but that in the steel is uniaxial. This choice reflects the fact that the rubber expands to fill the space, and touches the cylinder walls, whereas the shims were slightly smaller than the bore of the cylinder so they could be inserted into it. If the shims and cylinder are treated as rigid ($k_{shims} = k_{cyl} = \infty$), Equation (D-1) reduces to

$$K = k_{test} h_r \qquad \text{(D-2)}$$

The cylinder had internal and external diameters of 1.476 and 3.0 inches, and E and ν were taken to be 30,000 ksi and 0.30, so its radial stiffness, k_{cyl}, was computed (Timoshenko, 1962) to be 21,000 ksi/inch. The axial stiffness of the four 11 gage shims, k_{shims}, was computed to be 62,500 ksi/inch. The typical test stiffness, k_{test}, was about 270 ksi/inch. That is, in this case, about two orders of magnitude less than the cylinder and shim stiffnesses, so the simpler Equation (D-2) can be used. The modeling error introduced by ignoring the deformations of the shims and cylinder is less than 1%, and is probably less than the experimental error in measuring k_{test}.

Young's modulus, E, and Poisson's ratio, ν, were then computed from the measured G and K values, using the standard equations

$$E = \frac{3G}{1 + G/3K} \qquad \text{(D-3)}$$

$$\nu = \frac{3K - 2G}{2G + 6K} \qquad \text{(D-4)}$$

The resulting values for each elastomer compound are defined in Table D-24. These values are strictly applicable only to small strain, linear elastic behavior, but they were used for a range of analyses performed in this research study.

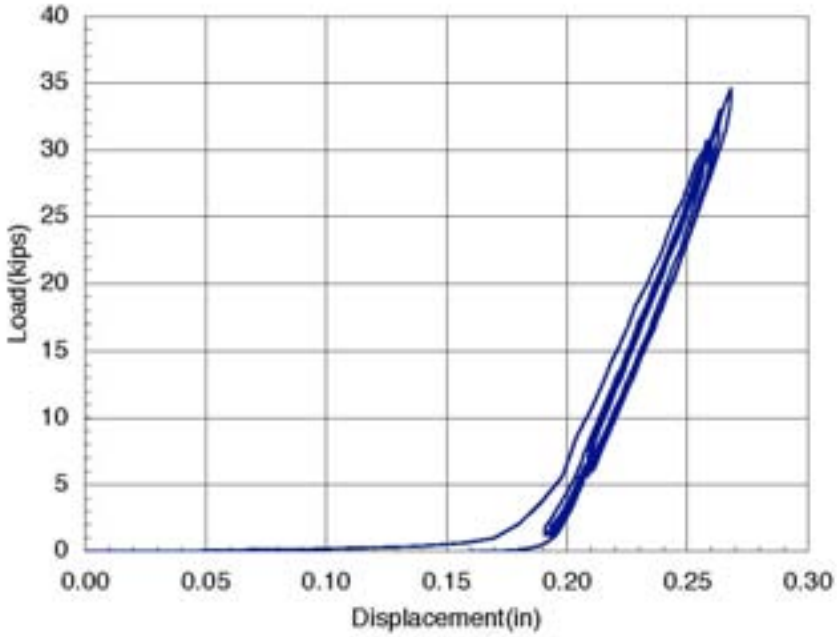

Figure D-43. Typical Load/Displacement Curve for Bulk Modulus Test

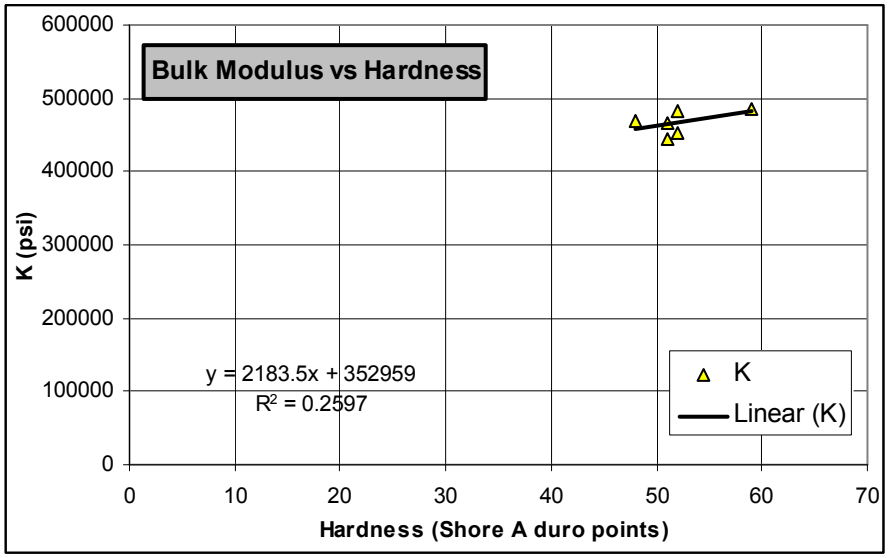

Figure D-44. Bulk Modulus vs. Hardness.

Bulk modulus values from Table D-24 are plotted as function of hardness in Figure D-44. Bulk modulus can be seen to be almost independent of hardness, which agrees with the findings of Holownia (1973).

D.3.2 Torsion Tests

A torsion test was developed for the purpose of estimating the extent of elastomer delamination during the rotation test program. Its design basis and details are described in Section C.4 of Appendix C. The torsion box initially was used to determine the torsional stiffness of each bearing before and after each rotation test to gauge how much of the rubber had delaminated from the steel plates. St. Venant torsion theory holds that a 1/2" deep separation along each long face of a 9-inch wide bearing would reduce the effective short dimension of the cross-section from 9 to 8 inches and therefore cause a drop in torsional stiffness to $(8/9)^3$ or 70% of its original value. Therefore, it was anticipated that the torsion box would be a sensitive measure of delamination damage.

However, the torsion box failed to show significant changes in stiffness for bearings that had obviously sustained serious damage. Therefore two measures were taken to test its effectiveness. First, a calibration test was completed. For this calibration, a bearing was physically delaminated by cutting the rubber to a known depth so that a 30% reduction in stiffness should occur. The damaged bearing was then tested and compared to its initial behavior. The results are shown in Figure D-45. The change in stiffness is negligible, and is certainly much less than the 30% predicted by theory. The reason for the discrepancy was never determined with certainty, but it was tentatively attributed to warping displacements in the rubber, which would cause the behavior to differ from that assumed in St Venant Torsion theory.

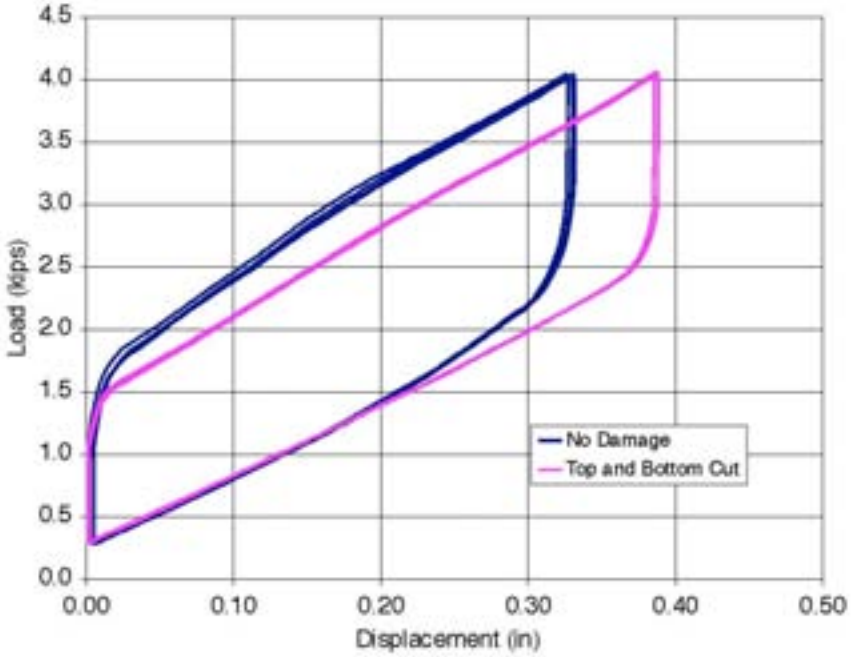

Figure D-45. Torsion Box Load/Displacement Curves Before and After Test CYC-14

A second check was performed by physically cutting open a number of tested bearings to determine how severely they were damaged during the cyclic rotation tests. This check showed that, in most of the specimens inspected, the debonding was limited to the edge of the shims, as shown in Figure D-16. Only when the cyclic rotational loading was

continued after 100% debonding had been reached did the separation propagate back into the body of the bearing. As a result, the use of the torsion box was discontinued, and all subsequent damage evaluation was conducted through direct measurements of bulge patterns and debonded length.

D.4 Analysis of Cyclic Rotation Data

The data from the cyclic tests were analyzed to extract trends in behavior in preparation for developing a design method.

D.4.1 Analysis Procedures

Throughout the cyclic rotation tests, data from the displacement sensors and load cells were recorded in order to gauge the material performance of each bearing. These data allowed determination of the stiffness and moment-rotation behavior of a bearing at all stages of the test. However, the body of the data was much too extensive to manually compare specific performance at different damage or deformation levels. As a result, a more automated evaluation process was developed, the results of which are provided in the detailed data summaries given in Appendix A. These computational procedures and evaluations are summarized here.

Shear strains in the elastomer were calculated in accordance with other recent research (Stanton and Lund, 2006). The maximum shear strain from axial load was calculated as:

$$\left|\gamma_{zx}\right|_{\max} = C_{czzx} S \varepsilon_{zz} = \frac{C_{czzx} S \sigma_{zz}}{E\left(1 + B_{az} S^2\right)} \tag{D-5}$$

where C_{azzx} is the coefficients for peak shear strain in the xz plane due to compression and B_{az} is the axial stiffness coefficient. These coefficients are functions of the aspect ratio and the compressibility index, λ,

$$\lambda = S\sqrt{\frac{E}{K}} \tag{D-6}$$

and were taken from the graphs provided in the paper. In Equation (D-6), S is the shape factor and E and K are the Young's modulus and bulk modulus. The maximum shear strain from rotation then was calculated as:

$$|\gamma_{zx}|_{\max} = \left|\gamma_{zx}\right|_{\max} = C_{ryzx} S \frac{L}{2} \frac{\theta_L}{t} \tag{D-7}$$

where C_{ryzx} is the coefficient for peak shear strain in the xz plane due to rotation, L is the length of the bearing, θ_L is the rotation per layer, and t is the layer thickness. The values of shear strain predicted by Equations (D-5) and (D-7) represent the tangent of the angle though which the material is sheared. Thus, for example, a shear strain of 1.3 represents a 1" thick element being displaced laterally by 1.3". Shear strains from all the cyclic tests were computed using Equations (D-5) and (D-7), and are tabulated in Table D-27.

Table D-27. Computed Response Values for Cyclic Rotation Tests.

Test	γAxial	γRot	Cycles to 50% Debond	Initial Rotational Stiffness (k-in/rad)	Stanton and Lund (2005) Rotational Stiffness (k-in/rad)	Ratio of Measured to Theoretical Stiffness	Stiffness Ratio at 50% Debond	EDC Ratio at 50% Debond	EVD Ratio at 50% Debond
CYC 5 A1	4.3	2.0	143	0.293	0.514	0.57	0.91	0.91	0.95
CYC 5 A2	4.6	2.1	531	0.282	0.467	0.60	0.78	0.74	0.92
CYC 5 B1	3.4	2.2	398	0.270	0.630	0.43	0.82	0.83	0.96
CYC 5 C1	3.7	1.8	156	0.365	0.605	0.60	0.74	0.83	1.04
CYC 5 D1	4.5	1.9	354	0.352	0.506	0.70	0.75	0.65	0.81
CYC 7 A1	4.1	1.3	1112	0.373	0.514	0.73	0.85	0.93	0.98
CYC 7 A2	4.4	1.4	1572	0.374	0.467	0.80	0.76	1.00	1.21
CYC 7 B1	3.4	1.5	2989	0.327	0.630	0.52	0.84	0.75	0.84
CYC 7 C1	3.6	1.3	3152	0.419	0.605	0.69	0.88	0.82	0.91
CYC 7 D1	4.4	1.2	1613	0.405	0.506	0.80	0.86	0.65	0.70
CYC 8 A1	4.1	0.8	2152	0.476	0.514	0.93	0.93	1.00	0.90
CYC 9 A1	5.2	1.8	124	0.306	0.514	0.60	0.97	1.00	1.04
CYC 9 A2	5.5	2.2	248	0.283	0.467	0.61	0.86	0.74	0.85
CYC 9 B1	4.6	2.1	398	0.284	0.630	0.45	0.87	0.88	0.98
CYC 9 C1	5.0	1.9	18	0.401	0.605	0.66	0.85	0.80	0.90
CYC 9 D1	6.3	1.9	192	0.425	0.506	0.84	0.74	0.76	0.95
CYC 11 A1	5.7	1.3	245	0.458	0.514	0.89	0.90	0.89	0.93
CYC 11 A2	6.1	1.2	320	0.445	0.467	0.95	0.85	0.77	0.86
CYC 11 B1	4.6	1.2	784	0.420	0.630	0.67	0.83	1.03	1.16
CYC 11 C1	5.1	1.2	408	0.522	0.605	0.86	0.83	0.73	0.82
CYC 11 D1	6.2	1.2	1396	0.491	0.506	0.97	0.81	0.59	0.67
CYC 12 A1	5.6	0.6	994	0.717	0.514	1.39	0.86	0.54	0.59
CYC 12 A2	5.9	0.5	19599	0.674	0.467	1.44	N/A	N/A	N/A
CYC 12 B1	4.7	0.6	62936	0.631	0.630	1.00	1.01	1.00	0.85
CYC 12 C1	5.0	0.6	45749	0.680	0.605	1.12	0.95	0.69	0.68
CYC 12 D1	6.0	0.5	191724	0.827	0.506	1.63	0.87	0.75	0.75
CYC 13 A1	4.1	0.3	N/A	0.592	0.514	1.15	1.00	1.00	1.00
CYC 14 A1	4.0	0.9	7105	0.355	0.514	0.69	1.00	0.91	0.91
CYC 15 C1	3.6	0.2	N/A	0.599	0.605	0.99	1.13	1.00	0.85
SHR 3 B1	3.1	1.5	39163	0.292	0.630	0.46	0.92	0.79	0.80
SHR 4 B1	3.3	1.9	181	0.243	0.630	0.39	1.02	N/A	N/A
SHR 5 B1	4.5	2.0	222	0.299	0.630	0.47	0.88	0.93	1.03
SHR 6 A2	5.5	0.9	21446	0.508	0.467	1.09	1.07	1.68	1.61
SHF 3 C2	2.9	1.7	4995	0.503	1.290	0.39	0.86	0.75	0.81
SHF 4 C2	3.8	1.8	6753	0.730	1.290	0.57	0.75	0.85	1.00
SHF 5 C2	3.8	1.0	N/A	0.729	1.290	0.57	0.96	0.71	0.71
SHF 6 C2	3.1	1.3	151930	1.085	3.201	0.34	0.84	0.78	0.82
ASR 2 C2	2.8	1.9	4369	0.192	0.389	0.49	0.60	0.54	0.80
ASR 3 C2	4.0	1.8	7188	0.255	0.389	0.66	0.66	0.56	0.74
ASR 4 C2	4.0	1.5	N/A	0.253	0.389	0.65	0.87	0.63	0.62
MAT 1 C2	3.1	1.8	793	0.392	0.743	0.53	0.81	0.61	0.69
MAT 2 C2	4.2	1.8	486	0.478	0.743	0.64	0.80	0.64	0.72
MAT 3 C2	4.1	1.1	6993	0.676	0.743	0.91	0.81	0.68	0.75
					Average	0.75	0.86	0.81	0.88

Moment-rotation plots were developed directly from the measured data. The moment was computed form the eccentric force applied by the MTS actuator (see Figure C-1), and the rotation was obtained from the LVDTs attached to the plates adjacent to the test bearing. The predicted moment about the y-axis, M_y, using linear theory was computed using the coefficients from (Stanton and Lund, 2006).

$$M_y = E\left(1 + B_{ry} S^2\right) I \frac{\theta_L}{t} \tag{D-8}$$

where B_{ry} is the rotational stiffness coefficient. Figure D-46 shows a typical measured moment-rotation curve. It takes the form of a loop, and displays some hysteresis, indicating that the material is slightly visco-elastic, and not truly elastic as assumed in the FE and closed form linear models. The moment-rotation curve derived from the linear theory, Equation (D-8), is also shown. It is a straight line, as should be expected for a linear elastic idealization. Measured and predicted rotational stiffnesses are presented, for all bearings subjected to rotational testing, in Appendix A.

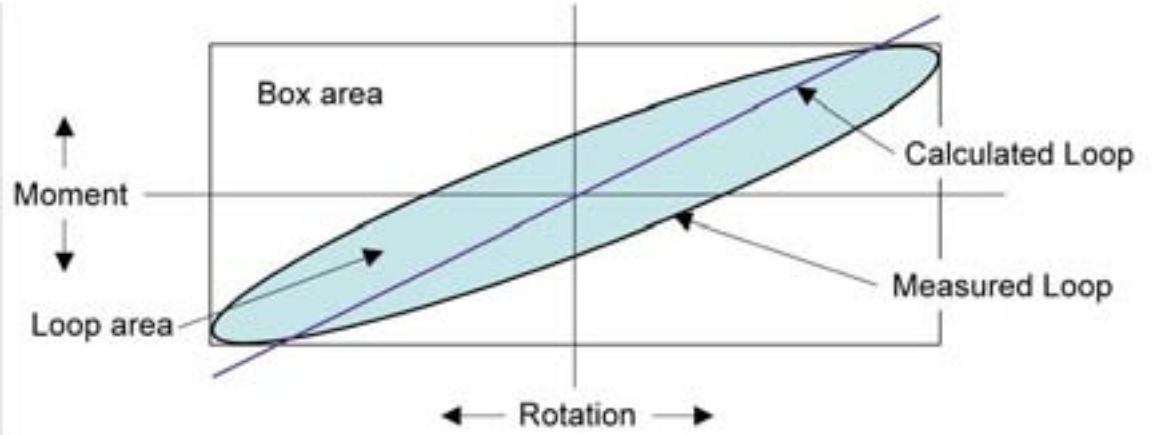

Figure D-46. Typical Cyclic Moment-Rotation Plot

In order to compare the measured and predicted rotational stiffnesses, it is necessary to derive a best-fit linear stiffness from the measured data. To achieve this, the measured data were first centered so that maximum and minimum moments were of equal magnitude. This was necessary because the self-weight of the rotational test rig components causes a small moment even when the rotation is zero. Then the best-fit linear stiffness that passed through the origin was found by using the least squared error criterion.

Measurements were not made continuously throughout the test, because of the huge amount of data that doing so would generate. Instead, two cycles of rotation were measured at regular intervals (every 60 to 200 cycles) throughout the test. The stiffness for each measurement set was the average over the two cycles. The individual measurement sets thus provided a detailed record of rotational stiffness over the course of the test. Also calculated was the stiffness from linear elastic theory:

$$K_r = \frac{E\left(1 + B_{ry} S^2\right)}{t} \tag{D-9}$$

The measured data were normalized with respect to the initial stiffness and are presented in Appendix A.

The area of the hysteresis loop in Figure D-46 is equal to the mechanical work done on the bearing per cycle. It limited the speed at which the tests could be run, because the energy was dissipated in the form of heat, and therefore raised the temperature of the bearing, as discussed in Section C.2.9. However, the energy dissipation rate was also viewed as a possible measure of damage or deterioration in the elastomeric bridge bearing. Two methods of addressing this issue were employed. They were the EDC (energy dissipated per cycle) and the EVD (equivalent viscous damping). The EDC was calculated as the area inside each moment-rotation loop as shown in Figure D-46.

$$EDC = \frac{1}{2} \sum_{i-1}^{n} \left(M_{i+1} + M_i\right)\left(\theta_{i+1} + \theta_i\right) \tag{D-10}$$

where M_i and θ_i are the moment and rotation, respectively, at point i along the moment-rotation curve. The EVD is then the ratio of the energy dissipated by the bearing to the energy applied to the system:

$$EVD = \frac{2}{\pi} \frac{EDC}{A_{rect}} \tag{D-11}$$

where

$$A_{rect} = \left(\theta_{\max} - \theta_{\min}\right)\left(M_{\max} - M_{\min}\right) \tag{D-12}$$

In Equation (D-11), A_{rect} is the area of the rectangle that circumscribes the loop, indicated as the "box area" in Figure D-46. These values were calculated for the two loops at each recording point, and are shown in Appendix A, normalized with respect to their initial values.

Table D-27 summarizes the computed results for the rotation tests. The first two columns show the peak shear strains due to axial force and rotation, calculated from the recorded data. The shear strain from axial load, γ_{Axial}, varies among tests with nominally identical compressive load for two reasons. First, these values are averaged from the axial load recorded over the whole test. The axial load varied in the early tests because of inevitable bleed-back in the hydraulic lines, but this was rectified in the later tests by developing and installing a servo-controlled regulation system for the axial load (see Section C2.3). Second, the tests were run before the shear modulus, *G*, of the individual bearings was known. These parameters combined to result in variation in the compressive shear strain, even though most tests were targeted for a given axial compressive shear strain level.

The shear strain from cyclic rotation, $\gamma_{Rotation}$, varies because these values were calculated from the readings of the LVDTs adjacent to the bearing, whereas the test was controlled

using the LVDT in the MTS actuator. These rotations are slightly different, because of the deformation of the lever arms of the test rig.

The third column shows the number of cycles to 50% debonding for each test. A value of N/A indicates that the bearing did not reach a level of 50% debonding. The fourth column shows the initial measured rotational stiffness, characterized by the least square best fit line, and the fifth is the predicted value from Equation (D-9). They are compared in the next column. The last three columns show the ratios of stiffness, EDC and EVD at 50% debonding to their initial values. In some cases the data are not available because the instruments slipped. For some tests that did not reach 50%, these three values are shown nonetheless, because the stiffness, EDC, and EVD reached a steady constant value and this was taken to be the value that would have been recorded at 50% debonding. The way that these values relate to damage is discussed in the following sections.

D.4.2 Shear Strains in the Elastomer

Most specifications limit the load and deformation capacity of an elastomeric bearing using the shear strain in the elastomer as the critical design parameter. Thus, efforts were made to link the nominal shear strains to the damage observed in the tests. The largest strain occurred on the compression side of each rotation cycle where the strain from axial load was added to the strain from rotation. The total strain to reach 25% and 50% debonding is plotted against number of cycles in Figure D-47 and Figure D-48. Figure D-49 and Figure D-50 show similar data, but for just the cyclic component of strain. The number of cycles is shown on a log scale not only to avoid crowding of the data near the vertical axis but also because the approach is commonly used with damage-related phenomena, such as fatigue.

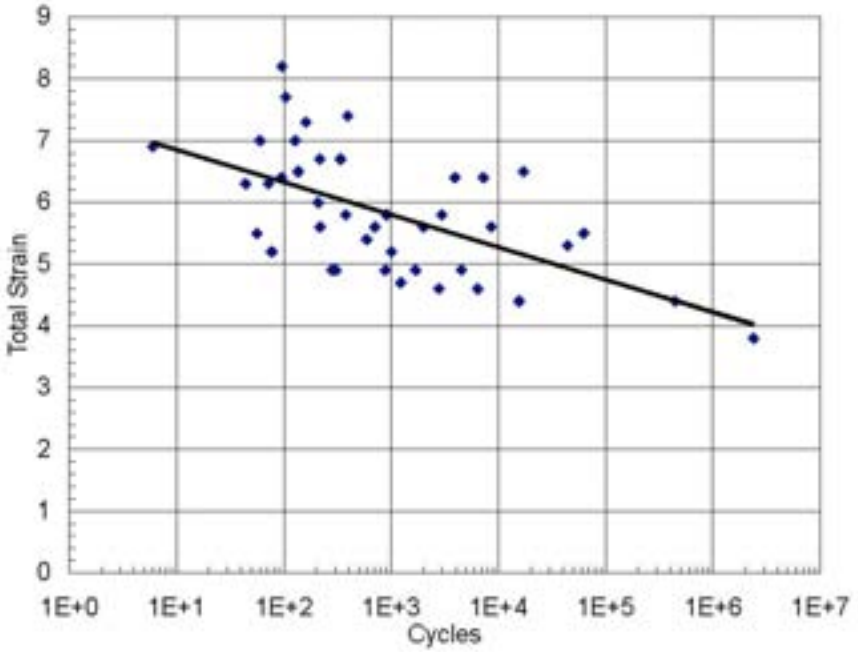

Figure D-47. Total Strain vs. Number of Cycles to 25% Debond

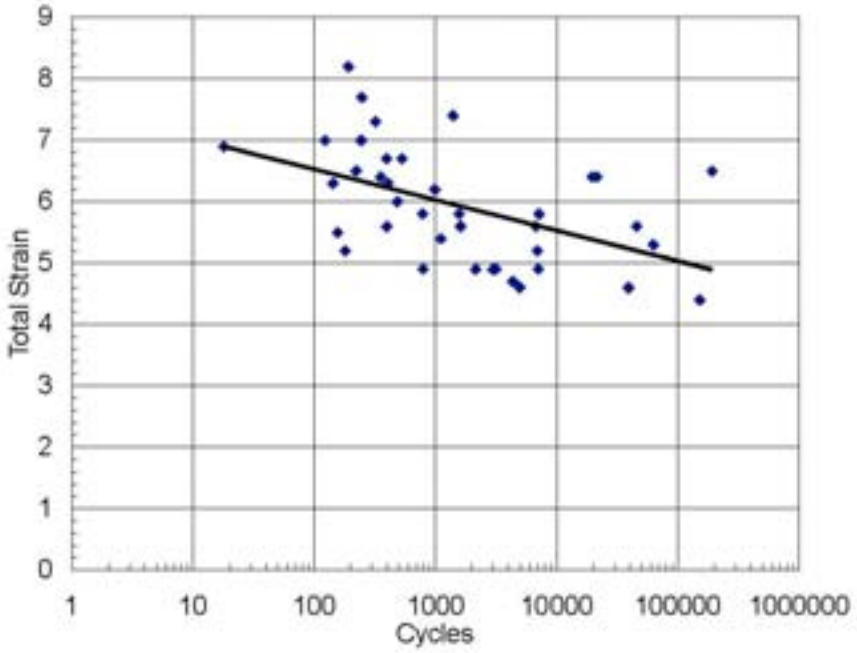

Figure D-48. Total Strain vs. Number of Cycles to 50% Debond

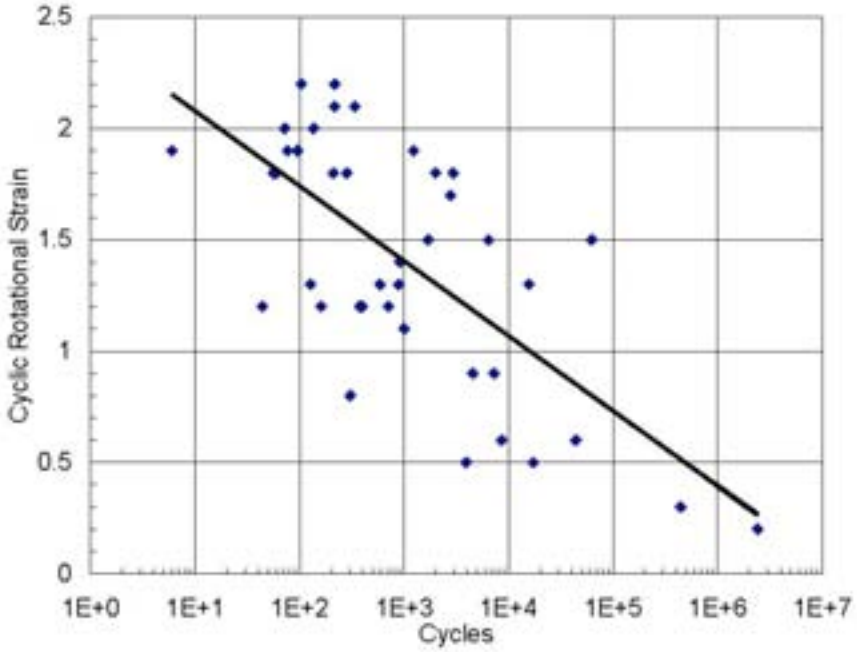

Figure D-49. Cyclic Rotational Strain vs. Number of Cycles to 25% Debond

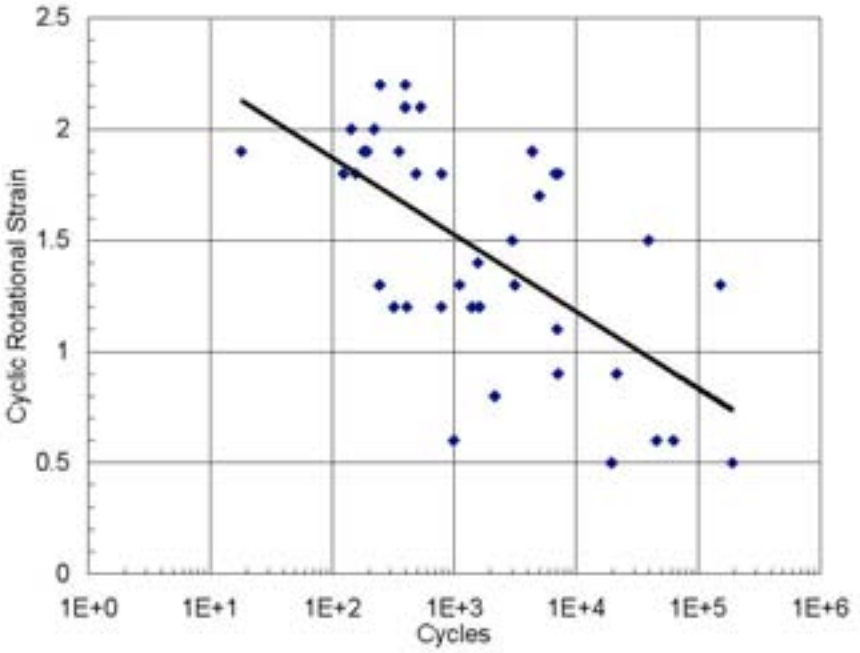

Figure D-50. Cyclic Rotational Strain vs. Number of Cycles to 50% Debond

There is considerable scatter in all four plots, but there is still a clear trend of decreasing shear strain capacity with increasing numbers of cycles. The correlation is not absolutely clear in any of the four plots, but it is clearly stronger in the plots where the cyclic rotational shear strain is plotted. It should be noted that the shear strain due to axial load is nominally constant for a given test, and so the observation that cyclic shear strain due to rotation provides a stronger correlation with the number of deformation cycles is an issue of importance in developing a design specification. This issue will be discussed in greater detail in a later section.

D.4.3 Rotational Stiffness

The torsion box test did not prove to be an accurate gauge of stiffness loss caused by damage to the bearing. As a result, variation in rotational stiffness was evaluated as a possible indicator of bearing damage. Figure D-51 shows the variation with cycle number of rotational stiffness for test specimen CYC-7-D1. The result for this specimen was typical of the general pattern. The stiffness clearly decreased as the test progressed, but the figure shows significant sudden increases in stiffness followed by gradual decreases. These increases correspond to the times when the test was paused. In general, the stiffness typically approached its original value when the test was paused for a significant period of time (such as an overnight delay) This indicates that the stiffness decreases are caused by material softening due to cyclic load rather than damage to the bearing. Further evidence of this hypothesis is provided by the fact that at 5,000 and 9,000 cycles, when the test was paused overnight, the rubber cover was nearly completely

debonded from the long edges of the steel plates. If no real loss of stiffness occurs even at full debonding, the rotational stiffness does not provide a good measure of damage in the bearing.

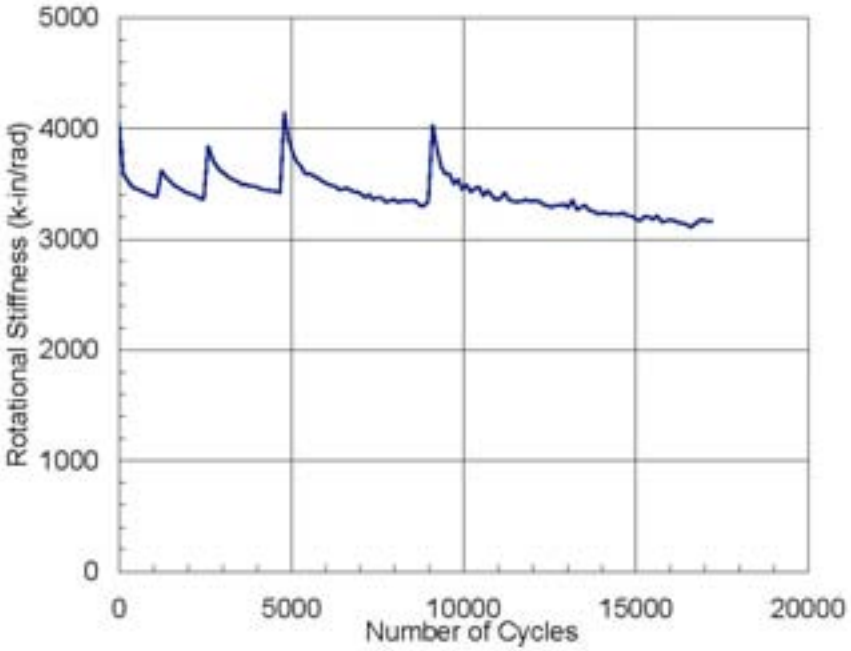

Figure D-51. Test CYC-7-D1 Stiffness Variations

D.4.4 Energy Dissipation - EDC and EVD

The energy dissipation measures, EDC and EVD, were analyzed with the goal of finding a relationship between them and bearing damage. Figure D-52 and Figure D-53 show the EDC and EVD vs. total strain, for all tests. Both quantities increase with total strain, even though considerable scatter exists. EDC is a measure of absolute energy dissipated and should therefore be expected to increase with strain. However, EVD is a relative measure of energy dissipation. In a system that is linearly visco-elastic, it would be independent of strain. The increase with strain shown in Figure D-53 shows that this is not the case for elastomeric bearings.

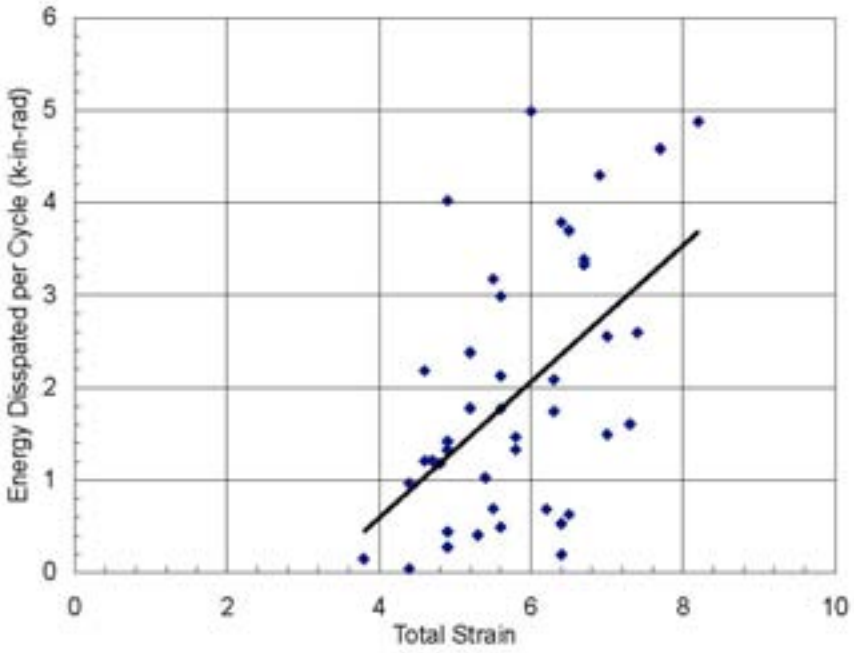

Figure D-52. Initial EDC vs. Total Strain for All Tests

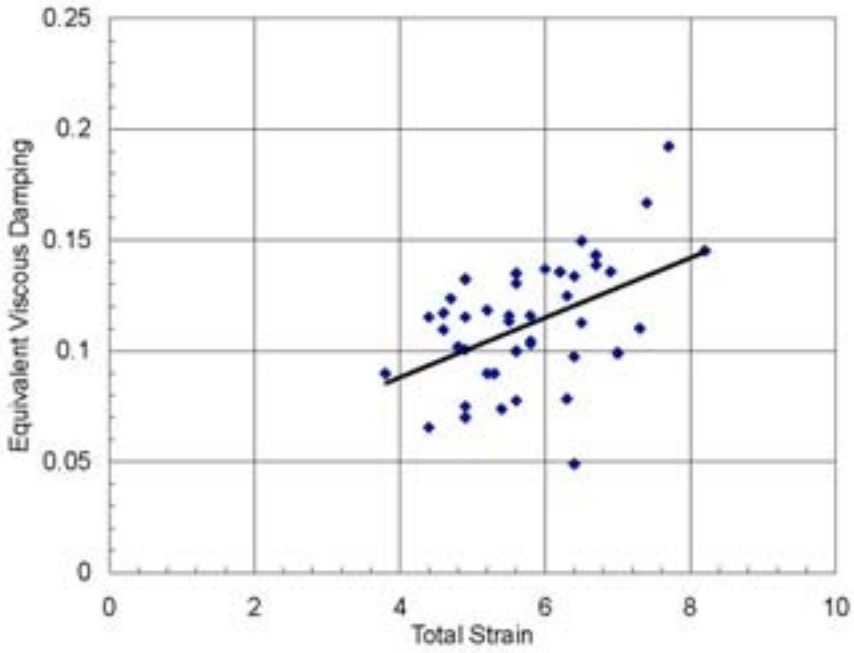

Figure D-53. Initial EVD vs. Total Strain for All Tests

Figure D-54 and Figure D-55 show EDC and EVD, normalized with respect to their initial values, as a function of the number of cycles to 50% debonding. They show that at 50% debonding, on average, the EDC and the EVD are 80% of their original values.

However, the large scatter and the correlation coefficients, -0.013 and 0.149, respectively, show that these relationships are not strong enough to be useful.

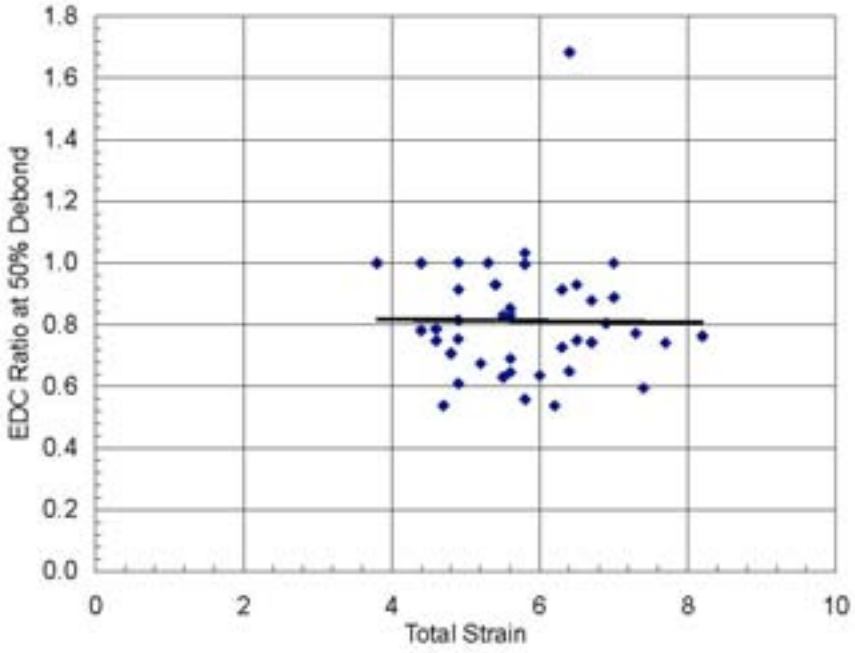

Figure D-54. Normalized EDC at 50% Debonding

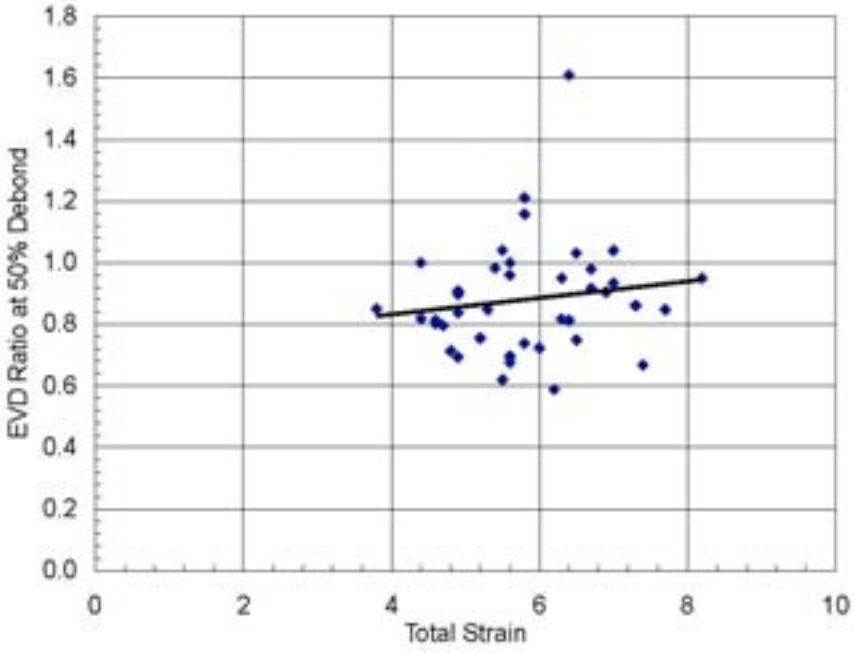

Figure D-55. Normalized EVD at 50% Debonding

D.5 Lift-off of the Bearing

Load combinations that include large rotations and small axial loads are important for elastomeric bearings, because they have the capacity to cause either reversal of shear strains at the edge of the bearing or net hydrostatic tension in the interior. Reversal of shear strain is believed to exacerbate fatigue damage (Cadwell et al. 1940), while hydrostatic tension is known to cause sudden and brittle rupture (Gent and Lindley 1959a). Both behaviors are undesirable.

The provisions for rotation in the existing AASHTO LRFD Specifications were developed without the benefit of a research study focused on that subject, and had to be prepared on the basis of the best information available at the time, and to err on the side of safety (Stanton and Roeder, 1982, Roeder, Stanton and Taylor, 1990). As a result, they were based on the concept of avoiding strain reversals by preventing net upwards movement of any point on the bearing. This results in the requirement

$$\theta < \frac{2\,\Delta_c}{L} = \frac{2\,\Delta_c\,t}{L} \qquad \text{(D-13)}$$

which is the basis for the existing Equation 14.7.3.5.1-1. It was also believed that this requirement also prevents hydrostatic tension. The requirement does indeed protect against both behaviors, but is does with a great deal of conservatism, and in doing so it creates difficulties for engineers faced with designing a bearing for construction conditions, where such load combinations usually occur.

In Appendix F, design provisions are developed that reduce the conservatism in two ways. First, they distinguish between "Lift-off", shown in Figure D-56, in which the sole plate is free to lift clear of the bearing over part of its surface, and "Uplift", as shown in Figure D-57, in which the bearing has external plates that, when rotated, can induce tension in the elastomer. Lift-off leads to, at worst, very local and small hydrostatic tension stresses that may occur close to the line along which the sole plate starts to separate from the bearing. They occur because bending of the outer shim is accompanied by out-of-plane shear, which requires tension in the elastomer for equilibrium. By contrast, uplift can easily induce hydrostatic tension stresses large enough to cause internal rupture. Treating the two differently is therefore both rational and important. Second, methods are developed in Appendix F for computing the value of the hydrostatic tension stress, and these were confirmed by the FE analysis in Appendix E. Calculating the value of the tension accurately, rather than using a conservative approximation, minimizes the problems for bearings with external plates, in which hydrostatic tension is a possibility.

Furthermore, the calculations of uplift in Appendix F showed that the sole plate will not separate from the bearing until the rotation reaches a value significantly larger than that defined in Equation (D-13).

As a result, all the cyclic tests were monitored for potential lift-off. In all cases, they had no external plates, so lift-off was possible if the rotation was large enough. However, lift-off was never observed in any cyclic test, but only in the monotonic rotation tests, in which the rotations were larger (up to 0.08 radians). Lift-off could not be detected using

instruments, but rather depended on careful visual observation, so it is possible that it occurred to a small degree in some cyclic tests, but simply was not noticed. (The monotonic tests not only used larger rotations, but they also ran much more slowly, providing more time to observe the response and to test with feeler gages for separation). However, the general tend of no lift-off in the cyclic tests supports the liberalization of the design requirements in such a way as to alleviate the artificial problems that now exist for bearings with no external plates under small axial load and large rotation.

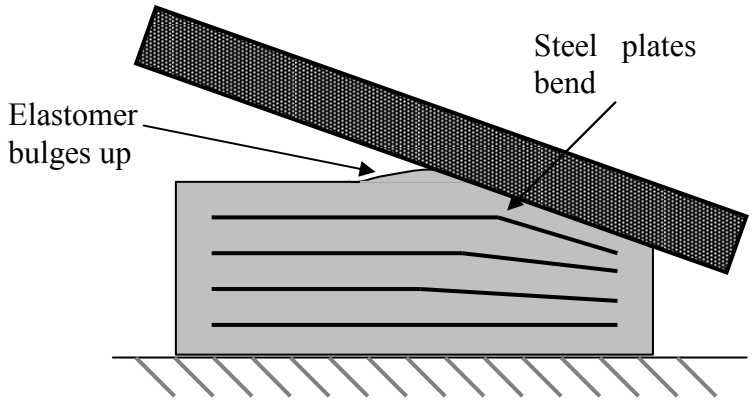

Figure D-56. Lift-off of the Bearing and Load Surface during Rotation

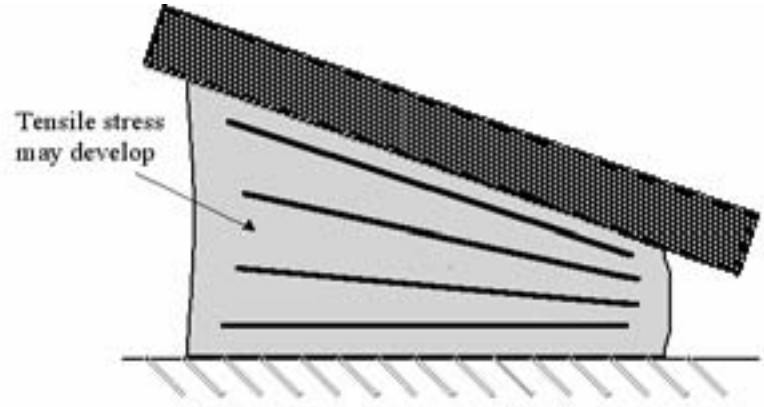

Figure D-57. Tensile Stress in Elastomer due to Uplift (Lift-off Prevented)

D.6 Summary and Conclusions on Test Program

This appendix provides an overview of the experimental test results, including comparisons between tests in order to show trends in behavior. Appendix A provides detailed numerical results for all test specimens. The most important observations from this appendix are summarized below.

D.6.1 Materials Testing

Standard materials tests were carried out by the manufacturers on specially prepared samples. The researchers also carried out bulk modulus and shear modulus tests on samples cut from the test bearings. All properties correlated only weakly with hardness (correlation coefficient < 0.32).

- Average shear modulus was 103 psi for the nominal 50 durometer samples, with a coefficient of variation of 33%. For the 60 durometer sample, it was 144 psi (40% higher). Shear modulus increased significantly with hardness.
- Average bulk modulus was 463 ksi for the nominal 50 durometer samples, with a coefficient of variation of 3%. For the 60 durometer sample, it was 485 ksi (5% higher). Thus, bulk modulus varied much less with hardness than did shear modulus, both among nominally identical samples and between samples with different nominal hardnesses. Overall, bulk modulus increased slightly with hardness.
- Average elongation was 585% for the nominal 50 durometer samples, with a coefficient of variation of 16%. For the 60 durometer sample, it was 428 % (26% lower). Elongation dropped significantly as the hardness increased.
- Average tensile strength was 2550 psi for the nominal 50 durometer samples with a coefficient of variation of 11%. For the 60 durometer sample, it was 2870 psi (12% higher). Tensile strength increased moderately with hardness.

D.6.2 Failure Criteria

Failure may occur through separation of the elastomer from the steel, fracture of the shims, brittle rupture of the elastomer through hydrostatic tension stress in the interior of the bearing or slip against the supporting medium. Shim fracture occurs only at axial stresses of about ten times the design axial stress, if shims of common thickness and strength are used. Existing specification provisions are able to predict it and protect against it adequately. Further protection is provided by the fact that the thickness of the shims are usually greater than required by the specifications in order to ensure that they remain plane during molding. Hydrostatic tension failure occurs only in bearings that have bonded external plates and that are subject to low axial compression and high rotation. Shim fracture and hydrostatic tension are thus expected to be rare, so separation of the steel from the elastomer represents much the most common form of damage.

- Separation of the elastomer from the steel shims may occur under compression, rotation or a combination of the two. It is initiated by debonding of the elastomer from the edges of the steel shims, defined here as debonding. Under more intense static loading or continued cyclic loading, the separation may propagate inwards

along, or close to, the surface of the shim. That process is referred to as delamination and is illustrated in Figure D-22. Edge debonding has little effect on the immediate performance of the bearing, but delamination has a significant adverse effect by making the bearing less stiff, particularly against vertical load, and by creating the possibility of the bearing eventually separating into two or more pieces. Delamination constitutes cause for replacing the bearing. Unfortunately, distinguishing between debonding and delamination is difficult from the outside of the bearing. The primary distinction lies in the size of the bulge.

- Hydrostatic tension was not observed in the tests, because all tests were conducted on bearings without external plates. Suitable methods of calculation are presented in Appendix F using closed form methods validated by Finite Element analyses.
- Shim fracture occurred in only two of the monotonic specimens, at an axial stress of 12 ksi. The other specimens reached the machine capacity (12 ksi) without shim fracture.
- Tests for slip were not conducted, because the results would be very different for elastomer in contact with smooth steel (in the rotation test rig) and with concrete or grout of unknown roughness (in the field). It was found that a slip-restraint system was needed to achieve rotations greater than about 4% in the test rig.

D.6.3 Methods of Measurement

Attempts were made with many different methods in order to find an objective way of evaluating damage caused by cyclic rotation. None was totally successful.

- A torsion rig was theoretically a promising candidate and one was developed and tried. However, the results from it proved very insensitive to the level of damage.
- The heights of the edge bulges in the bearing layers were measured using a micrometer depth gage. However, the Finite Element analyses showed that the bulge height was only weakly correlated with the internal strains. Furthermore, the slip restraints in the test rig obscured the outer edges of the bearing, where the baseline for the bulge height should be measured. This made reliable measurements difficult.
- Average stiffness over a cycle, energy dissipated per cycle and equivalent viscous damping were all investigated, but were found to have almost no correlation with damage accumulation. In particular, the stiffness was found to vary significantly when the testing was paused to take photographs, or overnight. These thixotropic changes swamped any others.
- Manual measurement of the length along the shims over which debonding had taken place was found to be the only viable method. The measurements were restricted to the two middle shims of the four in each bearing, because the outer two were largely hidden by the slip restraint bars in the test rig.

D.6.4 Monotonic and Low-cycle Axial Behavior.

Axial load tests were carried out under monotonic or low-cycle axial loads, in some cases accompanied by static rotation. These tests were conducted in a 2400 kip capacity Universal Test Machine, with tapered plates as needed for the rotation.

- All the axial load-deflection curves were highly stiffening-nonlinear. Establishing a true zero for the deflection posed problems, which in turn made calibration of models for axial behavior difficult.
- The peak deflection increased with each cycle. However, the increase was much the largest between the first and second cycles. The increase was attributed to debonding damage and decrystallization of the elastomer. The extent to which each contributed is not known with certainty, but the decrystallization is believed to have been the more important.
- Monotonic tests were carried out on bearings with S = 6. The specimens that performed the best did not debond at all when they reached the machine capacity of 12 ksi. In the worst performance, debonding initiated at a stress of 4200 psi, or 5GS. Low-cycle cyclic loading (to about 20 cycles) increased the extent of debonding.
- Shape factor played an important role. Bearings with S = 9 and S = 12 were tested. No debonding was observed in any of them, at the machine capacity of 12 ksi.

D.6.5 Cyclic Rotation

78 cyclic load tests were carried out. Each lasted between one day and three weeks. Various parameters such as axial load/rotation combinations, shear displacements, manufacturer, etc., were used to create the test matrix. Damage was measured in terms of the total length of shim over which debonding had occurred, and was recorded as a function of the number of cycles. The effects of different parameters on behavior are summarized below.

D.6.5.1 Bearing Manufacturer

- Nominally identical bearings from each manufacturer were subjected to the same eight tests (PMI-1a, 1b, 5, and CYC-5, 7, 9, 11 and 12). Each test defined a particular combination of constant axial load and cyclic rotation. Within any one test program, considerable scatter existed among the results of different specimens. However, no one manufacturer stood out as producing bearings that were more resistant than those of the others to fatigue damage. In all cases the axial loads and rotations used were significantly larger than those expected in practice. This was necessary to keep the tests short enough to be tractable.

D.6.5.2 Effects of Loading

- Cyclic rotations caused significantly more damage than static rotations of the same magnitude.
- Shear strain was induced by both the axial load and the rotation. The larger the strain, the more rapidly the damage accumulated.
- One test was run using a cyclic rotation of +/- 0.0125 radians. This was the smallest value used, but is still five to ten times the expected rotation in a bridge. That specimen did debond partially, but it only reached 25% debonding after approximately 2.4 million cycles. Thus no load combination was found that would lead to an endurance limit, i.e. no debonding after the expected life of the bridge (approximately 50 million cycles). Running such a test would anyway have taken approximately one year.
- Two tests were conducted with a fixed, static rotation on top of which the cyclic rotation was superimposed. By comparing the results with those of other tests in which the peak (total) rotation was the same, it was found that the cyclic component contributed much more than the fixed component to the debonding damage.
- Shear displacements were added to the axial load and rotation in four tests. The amplitude of the shear deformations was limited to 30% by the friction available between rolling steel components in the rig. The change in damage accumulation caused by the addition of 30% shear deformation was not perceptible within the scatter of the results. Previous experimental studies have shown that cyclic shear deformations can cause debonding. However, cyclic shear deformations are usually caused by thermal effects, which cause many fewer cycles than do traffic effects.
- In none of the cyclic load tests did the steel loading plate separate ("lift off") from the bearing, despite the relatively large rotations used in the test program. This finding suggests that the lift-off requirements in the current AASHTO Specifications merit review.

D.6.5.3 Effects of Bearing Characteristics

- Material properties. Three bearings were fabricated with a stiffer material (60 instead of 50 durometer), and tested with the same load combinations as tests CYC-5, 9 and 11. They displayed less debonding at any given number of cycles than did their 50 durometer counterparts. This better behavior may be explained in part by the fact that the axial forces imposed were the same as for the 50 durometer bearings, so the axial strains, and hence the shear strains, were smaller. However, comparison with bearings subjected to other axial load/rotation combinations suggests that the axial load does not explain the whole difference. The better performance was achieved despite the fact the material had a significantly smaller elongation at break, and adhesion, than the 50 durometer material from the same manufacturer. Elongation at break has in the past been taken as an indicator of shear strain capacity in a bearing.

- Shape factor. Three bearings with S = 9 and one with S = 12 were tested in cyclic rotation. They were made from the 60 durometer material. The imposed axial stress was selected to give the same shear strain as in the S = 6 bearings of the same material, so the axial loads were higher. All the high shape factor bearings performed very well. The S = 9 bearings took 7 to 13 times as long as the comparable S = 6 bearing to reach a given level of damage, while the S = 12 bearing took 128 times as long. Theory shows that a high shape factor should increase axial capacity but decrease the bearing's ability to accommodate rotation.
- Aspect ratio. The effects of aspect ratio were studied by testing three square bearings (aspect ratio = 1.0) made from 60 durometer material. They took 5 to 63 times as long as the comparable 9" x 22" bearings to reach a given level of damage, depending on the load combination. While theory shows that the square bearings should fare slightly better than the 22" x 9" bearings, the difference in performance was larger than predicted.
- Shim edge treatment. Bearings were tested with shims that had their edges prepared in three different ways: one set with as-sheared metal, one in which the shims were de-burred with a belt sander, and one with edges machined to a perfect semi-circle. The ones with the sharp, as-sheared, edges debonded faster than the other two, which performed in approximately the same way. This was particularly true for initial damage levels.